The Astrophysical Journal, 983:137 (28pp), 2025 April 20 https://doi.org/10.3847/1538-4357/adbb69

Tracing the Earliest Stages of Star and Cluster Formation in 19 Nearby Galaxies with PHANGS-JWST and HST: Compact 3.3 μm Polycyclic Aromatic Hydrocarbon Emitters and Their Relation to the Optical Census of Star Clusters

M. Jimena Rodríguez[1,2,3], Janice C. Lee[1,2], Remy Indebetouw[4,5], B. C. Whitmore[1], Daniel Maschmann[1,2], Thomas G. Williams[6,7], Rupali Chandar[8], A. T. Barnes[9], Oleg Y. Gnedin[10], Karin M. Sandstrom[11], Erik Rosolowsky[12], Adam K. Leroy[13], David A. Thilker[14], Hwihyun Kim[15], Jiayi Sun[16,30], Ralf S. Klessen[17,18], Brent Groves[19], Aida Wofford[11,20], Médéric Boquien[21], Daniel A. Dale[1,22], Leonardo Úbeda[1], Kirsten L. Larson[23], Kathryn Grasha[24,25,31], Kelsey E. Johnson[26], Rebecca C. Levy[2,32], Frank Bigiel[27], Hamid Hassani[12], and Sumit K. Sarbadhicary[13,28,29]

[1] Space Telescope Science Institute, 3700 San Martin Drive, Baltimore, MD 21218, USA; jrodriguez@stsci.edu
[2] Steward Observatory, University of Arizona, 933 North Cherry Avenue, Tucson, AZ 85721, USA
[3] Instituto de Astrofísica de La Plata, CONICET–UNLP, Paseo del Bosque S/N, B1900FWA La Plata, Argentina
[4] University of Virginia Astronomy Department, P.O. Box 400325, Charlottesville, VA 22904, USA
[5] National Radio Astronomy Observatory, 520 Edgemont Road, Charlottesville, VA 22903, USA
[6] Sub-department of Astrophysics, Department of Physics, University of Oxford, Keble Road, Oxford OX1 3RH, UK
[7] Max-Planck-Institut für Astronomie, Königstuhl 17, D-69117 Heidelberg, Germany
[8] Ritter Astrophysical Research Center, University of Toledo, Toledo, OH 43606, USA
[9] European Southern Observatory (ESO), Karl-Schwarzschild-Straße 2, 85748 Garching, Germany
[10] Department of Astronomy, University of Michigan, Ann Arbor, MI 48109, USA
[11] Department of Astronomy & Astrophysics, University of California, San Diego, 9500 Gilman Drive, La Jolla, CA 92093, USA
[12] Department of Physics, University of Alberta, Edmonton, AB T6G 2E1, Canada
[13] Department of Astronomy, The Ohio State University, Columbus, OH 43210, USA
[14] Department of Physics and Astronomy, The Johns Hopkins University, Baltimore, MD 21218, USA
[15] Gemini Observatory/NSF's NOIRLab, 950 North Cherry Avenue, Tucson, AZ, USA
[16] Department of Astrophysical Sciences, Princeton University, 4 Ivy Lane, Princeton, NJ 08544, USA
[17] Universität Heidelberg, Zentrum für Astronomie, Institut für Theoretische Astrophysik, Albert-Ueberle-Straße 2, D-69120 Heidelberg, Germany
[18] Universität Heidelberg, Interdisziplinäres Zentrum für Wissenschaftliches Rechnen, Im Neuenheimer Feld 205, D-69120 Heidelberg, Germany
[19] International Centre for Radio Astronomy Research, University of Western Australia, 7 Fairway, Crawley, 6009 WA, Australia
[20] Instituto de Astronomía, Universidad Nacional Autónoma de México, Unidad Académica en Ensenada, Km 103 Carr. Tijuana-Ensenada, Ensenada 22860, Mexico
[21] Université Côte d'Azur, Observatoire de la Côte d'Azur, CNRS, Laboratoire Lagrange, 06000, Nice, France
[22] Department of Physics and Astronomy, University of Wyoming, Laramie, WY 82071, USA
[23] AURA for the European Space Agency (ESA), Space Telescope Science Institute, 3700 San Martin Drive, Baltimore, MD 21218, USA
[24] Research School of Astronomy and Astrophysics, Australian National University, Canberra, ACT 2611, Australia
[25] ARC Centre of Excellence for All Sky Astrophysics in 3 Dimensions (ASTRO 3D), Australia
[26] Department of Astronomy, University of Virginia, Charlottesville, VA 22904, USA
[27] Argelander-Institut für Astronomie, Universität Bonn, Auf dem Hügel 71, 53121 Bonn, Germany
[28] Department of Physics, The Ohio State University, Columbus, OH 43210, USA
[29] Center for Cosmology & Astro-Particle Physics, The Ohio State University, Columbus, OH 43210, USA
Received 2024 August 3; revised 2025 February 26; accepted 2025 February 26; published 2025 April 15

Abstract

The earliest stages of star and cluster formation are hidden within dense cocoons of gas and dust, limiting their detection at optical wavelengths. With the unprecedented infrared capabilities of JWST, we can now observe dust-enshrouded star formation with ∼10 pc resolution out to ∼20 Mpc. Early findings from PHANGS-JWST suggest that 3.3 μm polycyclic aromatic hydrocarbon (PAH) emission can identify star clusters in their dust-embedded phases. Here, we extend this analysis to 19 galaxies from the PHANGS-JWST Cycle 1 Treasury survey, providing the first characterization of compact sources exhibiting 3.3 μm PAH emission across a diverse sample of nearby star-forming galaxies. We establish a selection criteria based on a median color threshold of F300M − F335M = 0.67 at F335M = 20 and identify 1816 sources. These sources are predominantly located in dust lanes, spiral arms, rings, and galaxy centers, with ∼87% showing concentration indices (CIs) similar to optically detected star clusters. Comparison with the PHANGS-HST catalogs suggests that PAH emission fades within ∼3 Myr. The Hα equivalent width of PAH emitters is 1–2.8 times higher than that of young PHANGS-HST clusters, providing evidence that PAH emitters are on average younger. Analysis of the bright portions of luminosity functions (which should not suffer from incompleteness) shows that young dusty clusters may

[30] NASA Hubble Fellow.
[31] ARC DECRA Fellow.
[32] NSF Astronomy and Astrophysics Postdoctoral Fellow.

increase the number of optically visible $\leqslant$3 Myr old clusters in PHANGS-HST by a factor between $\sim$1.8$\times$ and 8.5$\times$.

Unified Astronomy Thesaurus concepts: Star formation (1569); Young star clusters (1833); Polycyclic aromatic hydrocarbons (1280); Star clusters (1567); Spiral galaxies (1560); James Webb Space Telescope (2291); Interstellar dust (836)

1. Introduction

The formation of star clusters, the timescales over which they clear the gas and dust from their natal interstellar environments, and the factors that may influence these processes—such as cluster stellar mass, parent molecular cloud properties, and greater dynamical environment—are key to understanding galaxy evolution and the observed properties of galaxies. Clusters are sites of intense massive star formation, and as they age, they inject energy, momentum, and heavy elements into their surroundings. This feedback can alter the structure and composition of the interstellar medium (ISM), regulating subsequent star formation and reshaping the galaxy's gas content (e.g., P. F. Hopkins et al. 2014; R. S. Klessen & S. C. O. Glover 2016; M. Chevance et al. 2020; M. Y. Grudić et al. 2021; E. Schinnerer & A. K. Leroy 2024 and references therein).

Previous studies, particularly those on the morphology of H II regions based on Hα imaging with the Hubble Space Telescope (HST; required to resolve ionized gas associated with clusters in most nearby galaxies) have estimated a timescale of $\sim$3 Myr for clusters to clear dust and gas from their surroundings (e.g., K. Hollyhead et al. 2015; S. Hannon et al. 2019, 2022). These clusters, which are detected in the optical with HST, have cleared enough of their natal dust to allow stellar photospheric emission, in particular from massive stars, to be observed. For these clusters, age and mass can be estimated based on our understanding of stellar evolution in the context of simple stellar populations (e.g., A. Adamo et al. 2017; J. A. Turner et al. 2021). Earlier evolutionary phases can be sufficiently dust-embedded that they are not detected in the UV, and the very youngest are not detected in the optical at all. Progress requires a large sample of young embedded clusters, selected at infrared (IR) or longer wavelengths to overcome the limitations of optical and UV observations and to provide statistically robust constraints on the timescales for clearing natal dust and gas across a range of environments.

The sensitivity and resolution of JWST NIRCam enable embedded clusters and their environments to be studied with unprecedented detail across a wide range of nearby ($\lesssim$20 Mpc) galaxies with a resolution of $\lesssim$10 pc. Very recent studies have used JWST IR observations to study dusty young clusters in select nearby galaxies (NGC 7496, NGC 1365, NGC 3351, NGC 628, and NGC 3256) using Paα, Brα, and/or 3.3 μm polycyclic aromatic hydrocarbon (PAH) emission (M. J. Rodríguez et al. 2023; B. C. Whitmore et al. 2023; S. T. Linden et al. 2024; A. Pedrini et al. 2024; J. Sun et al. 2024). Notably, these studies also report short dust-clearing timescales of a few Myr, consistent with findings from HST Hα observations.

In our own work early in the JWST mission (M. J. Rodríguez et al. 2023), we demonstrated that 3.3 μm PAH emission is a particularly powerful tracer of the youngest star clusters, which remain enshrouded in dust and gas and are undetected in optical HST observations. We studied a sample of compact 3.3 μm PAH emitters in the spiral galaxy NGC 7496, the first galaxy to be observed for the PHANGS-JWST Cycle 1 Treasury program (J. C. Lee et al. 2023; T. G. Williams et al. 2024) in 2022 July.

PAHs are molecules composed of hydrogen and carbon atoms arranged in multiple aromatic rings. They are found in diverse environments including molecular clouds, disks around young stars, the diffuse ISM, star-forming regions, H II regions, and planetary and reflection nebulae. PAHs play a pivotal role in galaxies, contributing up to 20% of their total IR luminosity (J. D. T. Smith et al. 2007). These molecules exhibit prominent IR emission features at wavelengths of 3.3, 6.2, 7.7, 8.6, 11.3, and 12.7 μm (e.g., A. Leger et al. 1989; A. G. G. M. Tielens 2008; A. Li 2020). This distinctive emission is produced by vibrational modes excited by the absorption of 5–15 eV ultraviolet (UV) photons (B. T. Draine & B. S. Hensley 2021 and references therein). Since most UV is emitted by intermediate and massive stars, PAHs have been studied as star formation indicators. This approach is effective near massive star formation regions but requires calibration for larger regions and those that include diffuse gas (e.g., R. C. Kennicutt & N. J. Evans 2012; F. Belfiore et al. 2023; L. Zhang & L. C. Ho 2023 and references therein).

The 3.3 μm PAH feature arises from a C–H stretching vibrational mode in small PAHs, which have limited heat capacities (W. A. Schutte et al. 1993), making them easily excited by single UV photons or susceptible to destruction. In addition, this feature generally requires more intense or harder radiation fields than longer-wavelength PAH features. Consequently, the 3.3 μm PAH emission is particularly sensitive to the radiation environment, providing a distinctive signature compared to other PAH emission features at longer wavelengths (R. Yamada et al. 2013).

The 3.3 μm PAH feature has not been as extensively studied as other PAH features (A. Li 2020). Spitzer's InfraRed Spectrograph (IRS) covered a spectral range between 5.2 and 38 μm. Although captured by the Spitzer InfraRed Array Camera (IRAC), the wide bandwidth of IRAC1 ($\sim$20%; $\delta\lambda/\lambda = 0.75/3.55$) was not useful for isolating the 3.3 μm emission.[33] Observations of this feature were previously carried out by AKARI (68.5 cm primary mirror) and the Infrared Space Observatory (ISO; 60 cm primary mirror). These studies provide most of our pre-JWST knowledge of the nature of this emission. Due to the small apertures of these earlier IR observatories, studies of the 3.3 μm PAH feature were largely restricted to the Milky Way and Magellanic Clouds or to spatially unresolved observations of the brightest galaxies and active galactic nuclei (AGN; H. W. W. Spoon et al. 2000; E. Sturm et al. 2000; J. H. Kim et al. 2012; A. Li 2020). To the best of our knowledge, the first attempts to use 3.3 μm PAH emission as a star formation indicator were based on AKARI spectra of a small number of star-forming galaxies (e.g., M. Imanishi et al. 2010; J. H. Kim et al. 2012; R. Yamada et al. 2013). Later T. I. Mori et al. (2014) found this emission in Galactic H II regions.

[33] https://irsa.ipac.caltech.edu/data/SPITZER/docs/irac/iracinstrumenthandbook/6/

Table 1
Parameters Used in the Source Detection and Number of Sources Detected

Galaxy	d (Mpc)	(1 pixel = X pc)	Box (pixels)	$N_{\rm F\ Peak}$	$N_{\rm SE}$	$N_{\rm SE-add}$	$N_{\rm total}$	F300M − F335M > 5σ
NGC 5068	5.2	1.59	54	136,547	30,691	327	136,874	96
IC 5332	9.01	2.75	31	43,845	11,992	50	43,895	30
NGC 0628	9.84	3.01	28	119,008	56,592	877	119,885	83
NGC 3351	9.96	3.04	28	80,583	64,513	5267	85,850	45
NGC 3627	11.32	3.46	25	79,559	112,383	40,699	120,258	105
NGC 2835	12.22	3.73	23	34,345	16,454	136	34,481	41
NGC 4254	13.1	4.0	21	106,078	108,340	22,009	128,087	188
NGC 4321	15.21	4.65	18	59,883	19,128	1023	60,906	154
NGC 4535	15.77	4.82	18	39,321	5073	189	39,510	49
NGC 1087	15.85	4.84	18	23,155	15,989	1765	24,920	112
NGC 4303	16.99	5.19	16	65,738	72,403	17,938	83,676	135
NGC 1385	17.22	5.26	16	34,268	17,179	1978	36,246	239
NGC 1566	17.69	5.4	16	27,318	21,898	3606	30,924	134
NGC 1433	18.63	5.69	15	71,194	6078	487	71,681	12
NGC 7496	18.72	5.72	15	8248	5327	559	8807	34
NGC 1512	18.83	5.75	15	41,319	20,884	1596	42,915	19
NGC 1300	18.99	5.8	15	39,210	8742	555	39,765	27
NGC 1672	19.4	5.93	14	72,109	34,974	2411	74,520	265
NGC 1365	19.57	5.98	14	22,142	15,542	2709	24,851	294

Note. The columns refer to the galaxy's name, distance (G. S. Anand et al. 2021; J. C. Lee et al. 2023; both from PHANGS-HST tip of the red giant branch measurements and compiled from the literature), physical scale corresponding to 1 pixel in the F335M image (NIRCam long-wavelength channel, $0\farcs063$ pixel^{-1}; https://jwst-docs.stsci.edu/jwst-near-infrared-camera/nircam-observing-modes/nircam-imaging#gsc.tab=0), box size used for the background estimation (in pixels corresponding to 85 pc), number of sources detected using *find_peaks*, number of sources detected using SExtractor, number of sources only detected with SExtractor, and number of sources in the combined catalog. The last column lists the number of objects detected with F300M − F335M > 5σ and F300M and F335M above the 5σ detection limits (see Section 4.1 and green points in Figure 2).

With JWST NIRCam, 3.3 μm PAH emission can be imaged using the F335M filter at resolutions of 2.6–10.6 pc (point-spread function, PSF, FWHM $0\farcs11$) for galaxies at 5–20 Mpc, the range covered by the PHANGS sample (J. C. Lee et al. 2023; T. G. Williams et al. 2024). Given the diffraction limit, JWST observations of the 3.3 μm feature also have 2–3 times better angular resolution than PAH features at longer wavelengths.

Here, we extend our initial study of compact sources with 3.3 μm PAH emission (M. J. Rodríguez et al. 2023) to the full sample of 19 galaxies from the PHANGS-JWST Cycle 1 Treasury Program, providing the largest study to date of embedded star clusters and their dust-clearing timescales. We aim to test the ∼2 Myr timescale inferred from our previous analysis of NGC 7496 using an order-of-magnitude larger sample spanning a range of diverse galactic environments. We identify compact 3.3 μm PAH sources and separate them from older IR-emitting sources (e.g., asymptotic giant branch, AGB, stars; planetary nebulae, PNe). With this expanded sample, we seek to characterize the observed properties of the youngest star clusters as traced by 3.3 μm PAH emission and gain insight into their evolutionary status through comparison with published catalogs of star clusters from PHANGS-HST and gas+dust maps from PHANGS-JWST and PHANGS Atacama Large Millimeter/submillimeter Array (ALMA). We compute the fraction of the compact 3.3 μm PAH emitters associated with young clusters identified in the PHANGS-HST survey (J. C. Lee et al. 2022; D. Maschmann et al. 2024) and the fraction that can be considered to be dust-embedded.

The outline of the paper is as follows. Section 2 provides an overview of the data employed in our analysis. The source detection and photometry procedure are detailed in Section 3, while Section 4 outlines the methods employed to identify the PAH emitters. The properties of these objects are explored in Section 5. The comparison of these objects with the clusters from HST cluster catalogs is presented in Section 6, and a discussion of our findings is presented in Section 7. Finally, our key conclusions are summarized in Section 8.

2. Data

2.1. Imaging Observations

This paper is based on data from three PHANGS-HST and JWST Treasury programs, which provide UV-IR imaging from 0.27 μm to 21 μm for 19 galaxies (J. C. Lee et al. 2022, 2023; R. Chandar et al. 2024).[34] This sample includes the 19 galaxies observed by PHANGS during JWST's first year of science operations, i.e., those with available data from all of the principal PHANGS surveys with HST, ALMA, and MUSE (A. K. Leroy et al. 2021; E. Emsellem et al. 2022; J. C. Lee et al. 2022). The galaxies are selected to be representative of star-forming main-sequence spiral galaxies with solar gas-phase metallicities. A full list of the galaxies and their properties can be found in J. C. Lee et al. (2023, Table 1). For convenience, this paper also provides the galaxy names and distances in Table 1.

IR observations with NIRCam and MIRI obtained through the PHANGS-JWST Cycle 1 Treasury program included imaging in eight filters spanning 2.0–21 μm (NIRCam: F200W, F300M, F335M, and F360M; MIRI: F770W, F1000W, F1130W, and F2100W). Details on the JWST observing strategy and data reduction procedures can be found in J. C. Lee et al. (2023) and T. G. Williams et al. (2024). We

[34] HST15654, PI: Lee; JWST2107, PI: Lee; HST 17126, PI: Chandar.

Table 2
JWST Observations

Filter	Detector	t_{exp} (s)	PSF FWHM (arcsec)	PSF FWHM (pixels)	Aperture Radius (arcsec)	Aperture Radius (pixels)	Aperture Correction (mag)
F200W	NIRCam	1202.5	0.066	2.129	0.124	4	−0.63
F300M	NIRCam	386.5	0.100	1.587	0.124	2	−0.68
F335M	NIRCam	386.52	0.111	1.762	0.124	2	−0.66
F360M	NIRCam	429.5	0.120	1.905	0.124	2	−0.67
F770W	MIRI	88.8	0.269	2.445	0.168	1.5	−0.75
F1000W	MIRI	122.1	0.328	2.982	0.209	1.9	−0.75
F1130W	MIRI	310.8	0.375	3.409	0.236	2.14	−0.75
F2100W	MIRI	321.9	0.674	6.127	0.420	3.8	−0.75

Note. PSF FWHM NIRCam: https://jwst-docs.stsci.edu/jwst-near-infrared-camera/nircam-performance/nircam-point-spread-functions. PSF MIRI: https://jwst-docs.stsci.edu/jwst-mid-infrared-instrument/miri-performance/miri-point-spread-functions.

use the v1p1 version of the PHANGS-JWST reduced images.[35] The basic characteristics of the PHANGS-JWST Cycle 1 imaging, including total exposure times and PSF size, are provided in Table 2.

The precursor Cycle 26 PHANGS-HST Treasury survey obtained near-UV (NUV), *U*, *B*, *V*, and *I* observations of a larger set of 38 galaxies from 2019 to 2021. The exposure times were ∼2200 s (NUV), ∼1100 s (*U*), ∼1100 s (*B*), ∼670 s (*V*), and ∼830 s (*I*). Exposure times varied depending on whether appropriate imaging was already available in the archive, and exact values for each galaxy are provided in D. Maschmann et al. (2024, Table 1).

Later, a companion HST Cycle 30 Treasury program obtained Hα narrowband imaging for the 19 galaxies studied here (R. Chandar et al. 2024). At the time the analysis was undertaken for this paper, Hα observations were completed for all galaxies except for NGC 4535 and the northern pointing for NGC 2835, which were scheduled to be reobserved due to a guide star acquisition failure.[36]

The HST images were drizzled with a pixel size of 0.″04. Note that the WFC3 UVIS PSF size in the *V* band is nominally 0.″067—comparable to the NIRCam PSF size[37]—though the resolution is degraded due to detector undersampling.

2.2. Star Cluster Catalogs

PHANGS-HST has recently completed the largest census to date of ∼100,000 optically selected star clusters and compact associations across 38 spiral galaxies (D. Maschmann et al. 2024; D. Thilker et al. 2024). Catalogs of the observed properties are available on the PHANGS High Level Science Product website at MAST.[38] These catalogs are the result of pipeline efforts described in J. C. Lee et al. (2022), which refined techniques for cluster candidate detection and selection (B. C. Whitmore et al. 2021; D. A. Thilker et al. 2022b), photometry (S. Deger et al. 2022), and automated morphological classification using machine learning techniques (W. Wei et al. 2020; B. C. Whitmore et al. 2021; S. Hannon et al. 2023).

Following M. J. Rodríguez et al. (2023), we use the PHANGS-HST cluster catalog to place our study of the early stages of star, cluster, and ISM evolution within the broader population that is no longer dust-enshrouded. The PHANGS-HST cluster catalog provides age, stellar mass, and dust reddening from spectral energy distribution (SED) fitting of five-band NUV, *U*, *B*, *V*, *I* photometry (J. A. Turner et al. 2021; D. Thilker et al. 2024). As effectively single-age populations, clusters serve as clocks to constrain the timescale of compact 3.3 μm PAH emission and, ultimately, the duration of the embedded phase.

The PHANGS-HST optically selected cluster census includes populations with ages spanning from ∼1 Myr to the age of the Universe and over four decades in stellar mass, up to $\sim 10^6\ M_\odot$. Separate catalogs are available for clusters that have been morphologically classified by humans and convolutional neural networks (W. Wei et al. 2020; B. C. Whitmore et al. 2021; S. Hannon et al. 2023). In this study, we consider clusters in both "human-classified" and "machine learning" catalogs that are classified as class 1 (symmetric compact cluster) and class 2 (asymmetric compact cluster). The number of clusters identified per galaxy is listed in D. Maschmann et al. (2024, Table 3). The number of human- (machine-) classified clusters in each of the 19 PHANGS-JWST galaxies studied here ranges from 182 to 774 (182 to 2828), with a median of 480 (777) and a total sample size of 8608 (21,353). We note that these numbers differ slightly from those listed in D. Maschmann et al. (2024) due to small variations in the HST and JWST footprints.

3. Source Identification and Photometry

3.1. NIRCam F335M Source Detection

Our procedures build on methods used to study dust-embedded star clusters in NGC 7496 (M. J. Rodríguez et al. 2023). We perform source detection on images taken with the NIRCam F335M filter, which captures the 3.3 μm PAH feature and the stellar continuum.

We use the *find_peaks* algorithm from the PHOTUTILS (L. Bradley et al. 2022) Astropy package to detect sources in the F335M image. This algorithm identifies local maxima above a specified intensity threshold and separated by a minimum number of pixels. We adopted a separation of 3 pixels, equivalent to 1.7 times the FWHM of the PSF in F335M (Table 2), which corresponds to ∼5–18 pc for the range of distance of the galaxies (Table 1). This choice effectively detects sources, particularly in crowded regions, where most objects of interest are located.

To determine appropriate local intensity threshold values, we produced 2D background images for each galaxy. We

[35] Available at https://archive.stsci.edu/hlsp/phangs.
[36] The Hα reduced and continuum-subtracted images will be released at https://archive.stsci.edu/hlsp/phangs.
[37] https://hst-docs.stsci.edu/wfc3ihb/chapter-6-uvis-imaging-with-wfc3/6-6-uvis-optical-performance
[38] https://archive.stsci.edu/hlsp/phangs

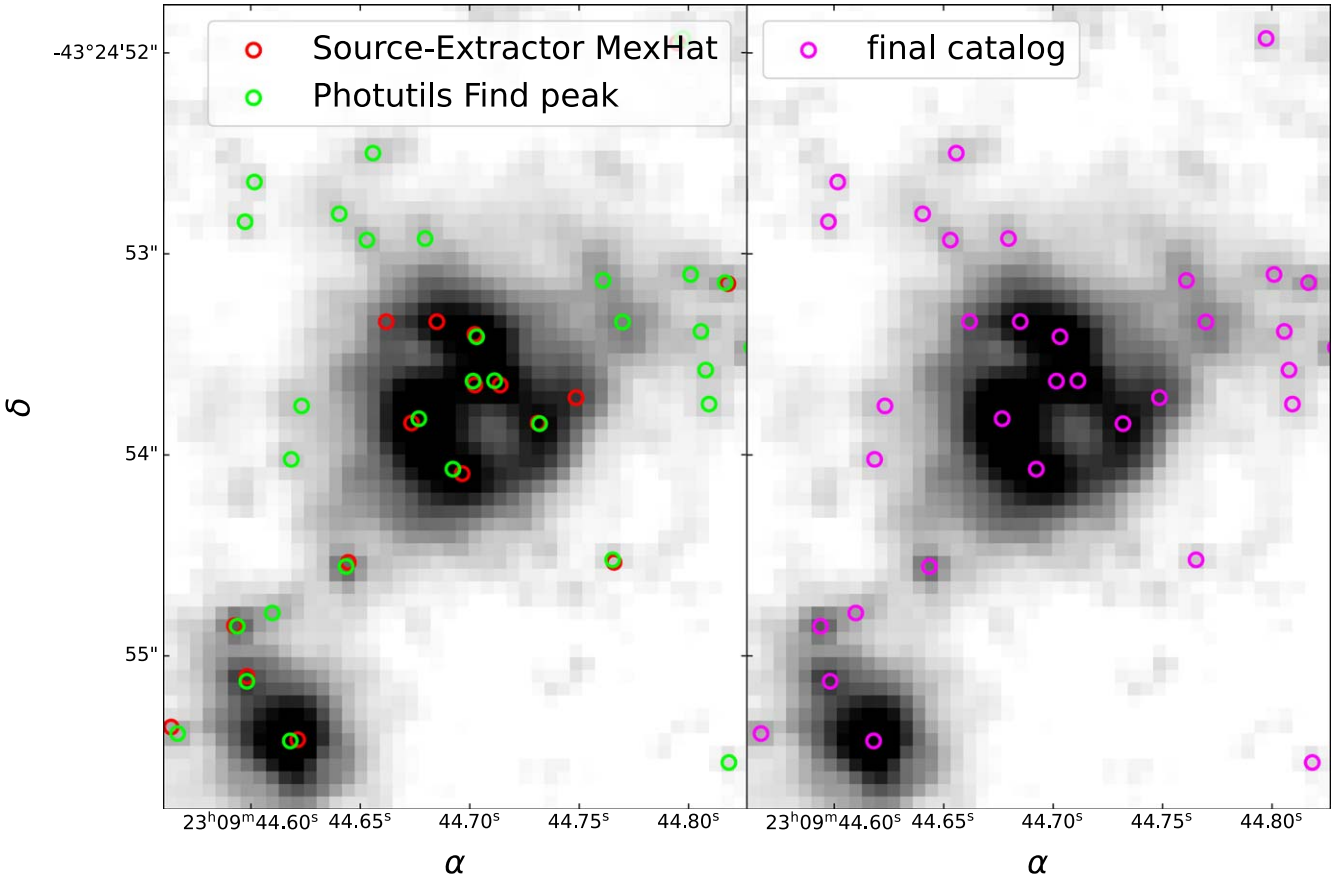

Figure 1. F335M image of a crowded region in the galaxy NGC 7496. The left panel displays the sources detected using both the *find_peaks* algorithm of Photutils and the SExtractor Mexican-hat filter. It is noticeable that SExtractor detects three sources (red circles) missed by *find_peaks* (green circles), which can be attributed to its better performance in deblending sources. In the right panel, we present the final catalog of sources for the same region, produced as a combination of the two aforementioned methods (see Section 3.1 for details).

estimated the background in boxes of 85 pc^2 using the *SExtractorBackground* function of Photutils. As described in the Photutils documentation,[39] the background in each box is calculated as $(2.5 \times \text{median}) - (1.5 \times \text{mean})$, except where $(\text{mean} - \text{median})/\text{std} > 0.3$, in which case the median is used instead.

The choice of background box size balanced several factors: the size should be larger than typical compact sources, small enough to capture the local variations of the background, and large enough to provide robust statistical estimates. Additionally, to be consistent across our galaxy sample, we choose a common physical box size that meet these criteria. To determine this box size, we tested different values in the galaxies NGC 628 (9.84 Mpc) and NGC 7496 (18.72 Mpc). After visually inspecting the results in these two galaxies, we found that using a box size in pixels corresponding to 85 pc (Table 1, column (4)) successfully identified all or most of the visually recognizable objects. In contrast, larger or smaller box sizes result in excessive noise detections or the loss of faint sources. Finally, the background image was processed with a median filter to suppress local overestimations or underestimations, such as those caused by bright regions within individual boxes. The detection threshold was set at the background level plus 3 times the sigma-clipped standard deviation.

[39] https://photutils.readthedocs.io/en/stable/index.html

Based on visual inspection (e.g., Figure 1, left panel), the *find_peaks* algorithm effectively detects faint and extended sources as well as bright, pointlike sources but tends to miss sources in crowded regions. In these regions, SExtractor (E. Bertin & S. Arnouts 1996) uses a Mexican-hat filter to produce improved results, since the algorithm includes the option for source deblending. Thus, we also run SExtractor using a Mexican-hat filter with 64 deblending subthresholds and the same background parameters used with the *find_peaks* method. In the left panel of Figure 1, we show the sources detected using *find_peaks* (green) and SExtractor (red) over a crowded region in the northern area of the galaxy NGC 7496. We can see that SExtractor detects three additional sources in the ring but does not capture many of the faint sources beyond the ring. For this reason, to construct the final source catalog, we combine detections from both algorithms. We perform a cross-matching of the source positions in both catalogs using a search radius of $0\farcs126$ (2 pixels in the F335M image), retaining all *find_peaks* detections and adding the sources detected only by SExtractor for the final source catalog. The right panel of Figure 1 shows the sources in the final catalog after the cross-correlation to merge both methods.

Table 1 lists the number of sources detected by each method, along with the number of sources detected only by SExtractor. Again, the number of sources in the final catalog is generally the number of sources identified by *find_peaks* plus those found only with SExtractor. The fraction of additional sources contributed by SExtractor

varies across galaxies, ranging from less than 1% in IC 5332 to 36% in NGC 3627 with a median of 8%.

3.2. Photometry and Aperture Corrections

We perform photometry using PHOTUTILS (L. Bradley et al. 2022) with circular apertures centered on the position of the sources detected in the F335M image, as described in the previous section. Photometry is measured in up to six HST and eight JWST filters. For HST, these include F275W, F336W, F438W or F435W, F555W, F658N or F657N and F814W. For JWST, the bandpasses are F200W, F300M, F335M, F360M, F770W, F1000W, F1130W, and F2100W.

For HST images, we use apertures with a radius of 0.″158 (equivalent to 4 WFC3 pixels) and background annuli that cover 0.″277 and 0.″356 (7–9 WFC3 pixels). These are the same aperture sizes used for the PHANGS-HST cluster catalog, which roughly correspond to the half-light radius of clusters (S. Deger et al. 2022). Similarly, for the NIRCam bands, we use a circular aperture with a radius of 0.″124, corresponding to 4 pixels in the NIRCam short-wavelength channel (F200W) and 2 pixels in the long-wavelength channel (F300M, F335M, F360M), and an annulus between 0.″248 and 0.″372. For the MIRI bands, the PSF is significantly larger (up to a factor of 10 larger for F2100W relative to F200W), and we simply adopt an aperture corresponding to 50% of the encircled energy[40] and an annulus between 2 and 3 times the size of the aperture. The background annulus width for both the NIRCam and MIRI bands is equal to the radius of the aperture as listed in Table 2. To exclude sources from the measurement of the background, we perform sigma clipping with a maximum of five iterations and reject values beyond 3σ. The flux density in the source aperture is then calculated by subtracting the median background value (scaled by the aperture area) from the total flux measured within the aperture. In this work, we only use the longer-wavelength photometry in F2100W and F1000W to impose a conservative color cut and remove a few percent of the sample as suspected red evolved stars (Section 4.2) and to qualitatively examine the shape of the SEDs of compact 3.3 μm emitters (Sections 4.3 and 7.1).

The standard procedure for computing the photometric error, which accounts for the Poisson noise and other noise sources that introduce uncertainty in measuring the background level, is an elementary calculation and well documented.[41] For photometry of bright sources and photometry in fields where the background is flat, the procedure is straightforward and involves adding the noise terms in quadrature. However, in cases where the background is not flat and exhibits large variations on the size scale of the aperture, the standard procedure may not be sufficient to provide a robust indicator of the photometric error. One such case is when an image is dominated by ISM emission (e.g., PAH emission, dust continuum emission, nebular emission) rather than stellar photospheric emission, and the standard photometric error may not allow us to discriminate whether a source is a true source or a local peak in the messy structure of the ISM.

In this context, we have tested other methods to derive more appropriate photometric uncertainties and adopted the most conservative approach for this work. For images where the signal is dominated by ISM emission (Hα and JWST images F300M and longer wavelengths), we compute the difference between the 90th and 10th percentiles of pixel values in the background annulus after sigma clipping. If the distribution is Gaussian, this calculation, when scaled by 4.6, will equal the standard deviation. However, if the distribution is non-Gaussian, the calculation will appropriately yield a larger uncertainty. Comparison of the scaled 90th–10th percentile width with standard photometric errors shows agreement for bright sources above the detection limit, where the Poisson noise of the source dominates the error. For bright sources in areas where the local background is high (e.g., in star-forming rings and in the central regions of galaxies, NGC 3351 is an example; see Section 5.1), the quoted uncertainty (which we know to be conservative) is higher by 2–3 times or more.

For HST imaging, we applied aperture corrections as described in detail in S. Deger et al. (2022) using a carefully selected sample of bright, isolated PHANGS-HST star clusters, including both young and old clusters. For NIRCam bands, we derived aperture corrections following the same procedure as in S. Deger et al. (2022) but for photometry obtained using a radius of 4 NIRCAM pixels (i.e., 0.″124) using isolated old globular clusters in NGC 628. The values (listed in Table 2) show good consistency ranging from 0.63 mag in F200W to 0.68 mag in F300M. This is similar to the average aperture correction from S. Deger et al. (2022; i.e., 0.67 mag), which is reasonable given the similar spatial resolution of NIRCAM's short-wavelength channel and HST. Only the brightest old globular clusters have sufficient IR flux in NIRCAM and MIRI to be used for this measurement.

For MIRI images, we applied a factor of 2.0 to the flux measurements from a circular aperture that captures 50% of the encircled energy of a point source. This simplification, compared to NIRCAM, is motivated by the much poorer spatial resolution of MIRI, which results in spatial profiles for clusters that are essentially the same as for stars. The source detection and photometry code used in this work can be found in the GitHub repository.[42]

4. Selection of Compact 3.3 μm PAH Emitters

4.1. Color–Magnitude Diagram and Sample Selection

Using the aperture-corrected photometry described in the previous section, we construct F335M versus F300M − F335M color–magnitude diagrams (CMDs) for all 19 PHANGS-JWST Cycle 1 galaxies (Figure 2). F335M captures the 3.3 μm PAH feature, while F300M primarily probes the stellar and dust continuum. In our previous work, we used this CMD to identify objects with significant PAH emission through detection of an F300M − F335M color excess (Figure 2 in M. J. Rodríguez et al. 2023). These CMDs are analogous to those used to select emission line galaxies in narrowband imaging surveys (e.g., C. Ly et al. 2011; J. C. Lee et al. 2012), and similar strategies can be adopted to identify and characterize stellar populations associated with PAH emission.

To select PAH emitters, we employ a combination of two thresholds: (1) the significance of the color excess and (2) the F335M and F300M detection limits. The locus of points around F300M − F335M ∼ 0 represents continuum sources with little

[40] https://jwst-docs.stsci.edu/jwst-mid-infrared-instrument/miri-performance/miri-point-spread-functions

[41] For example, https://www.stsci.edu/instruments/wfpc2/Wfpc2_hand_current/ch6_exposuretime6.html.

[42] https://github.com/JimenaRodriguez/Phangs-photometry

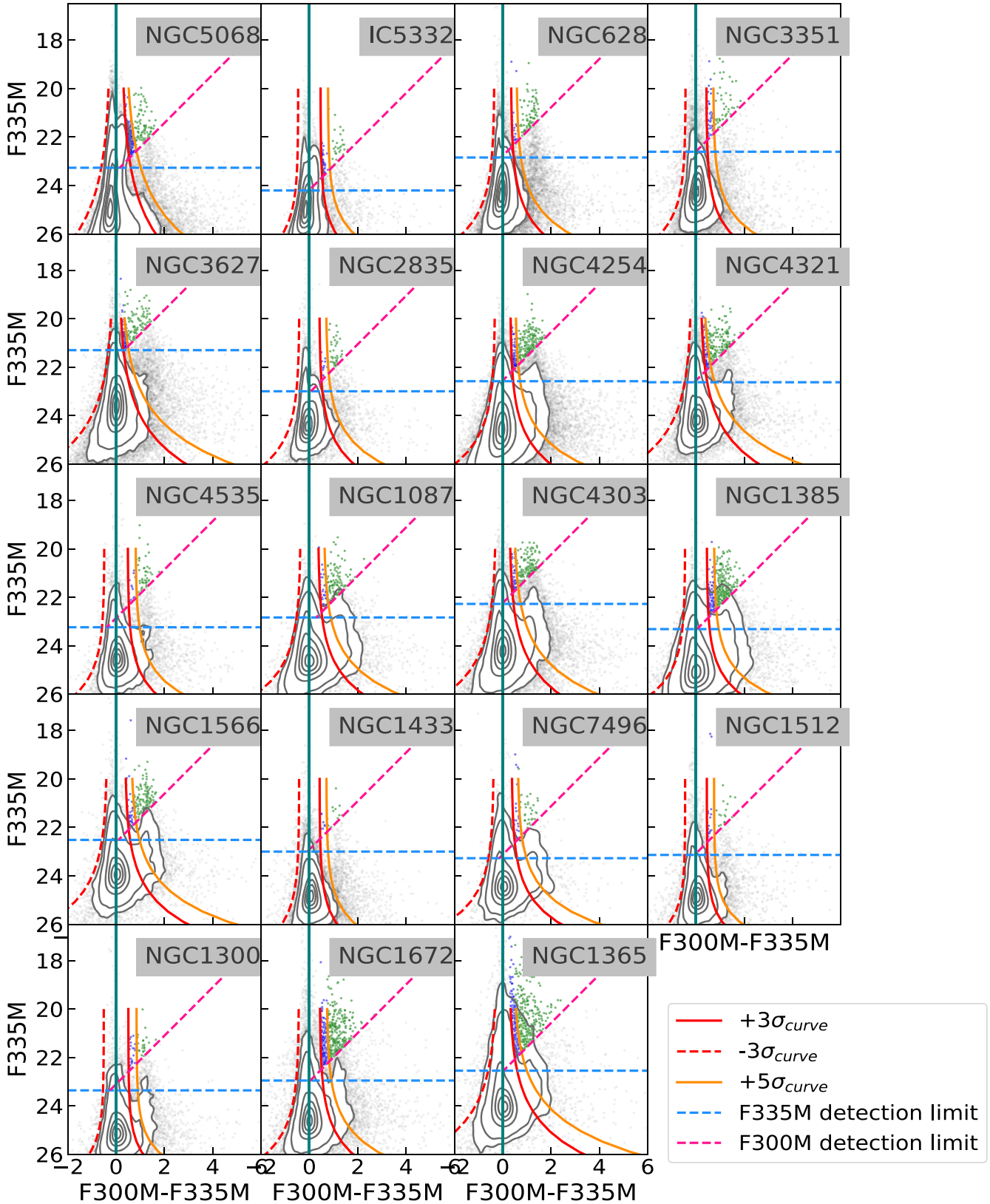

Figure 2. CMDs F335M vs. F300M − F335M for the 19 galaxies included in the PHANGS-JWST Cycle 1 Treasury program. The plots are organized by increasing galaxy distance from the upper left corner to the bottom right. The contours represent the 5th, 10th, 30th, 50th, 70th, and 90th density percentiles. The small gray dots indicate regions where the density is lower than the 5th percentile. The red and orange curves indicate $\pm 3\sigma$ and $+5\sigma$ in color dispersion, respectively. The dashed horizontal light blue line indicates the adopted F335M detection limit for each galaxy, while the F300M limit is shown with a dashed pink line. These values were derived from 5σ measurements relative to the mean obtained via random apertures. The vertical line indicates F300M − F335M = 0. The blue dots show sources with color excess between 3σ and 5σ, while the green dots are sources with F300M − F335M $> 5\sigma$ and comprise our primary compact PAH emitter sample.

to no PAH emission. The distribution of continuum sources broadens at fainter F335M magnitudes due to increasing noise in the F300M − F335M measurement (compare with Figure 3 in J. C. Lee et al. 2012, and see Section 3.2). To select sources with significant color excess relative to the combined intrinsic color spread plus noise, we assume symmetry in the color distribution of continuum sources and measure the dispersion of negative F300M − F335M values in bins of F335M. We then determine the 1σ color dispersion curve by fitting an exponential function of the form $\sigma_{(\mathrm{F300M-F335M})} = ae^{b(\mathrm{F335M})} + c$. The curves in Figure 2 represent 3σ and 5σ color dispersion values computed in this way.

We select a primary sample of compact PAH emitters above a 5σ color dispersion (green points in Figure 2). The number of objects in this sample is listed in the last column of Table 1. Sources with a color excess between 3σ and 5σ are also highlighted in Figure 2 (blue points). Later in the paper, we examine whether there are differences in the properties of these weaker PAH emitters.

The 5σ F335M and F300M detection limits for each galaxy are derived by measuring photometry using 500 randomly positioned apertures on the F335M and F300M images, respectively, and computing the dispersion of the resulting distribution of measurements. This procedure uses the same aperture size and aperture correction as the photometry of the sources (see Table 2). The F335M limit is shown as a dashed horizontal light blue line in Figure 2, while the F300M limit is represented by the dashed pink line.

There is considerable variation in the F335M detection limit from galaxy to galaxy—the median 5σ detection limit is 23.6 AB mag with a range of 22.0–24.9. Computing the detection limit for stars and clusters in PHANGS imaging is complex, as these compact structures must be detected above the background light of the galaxy, which can be highly nonuniform. This threshold is inherently higher and more variable across galaxies (and indeed among different regions within the galaxies themselves) than a limit based on the instrumental and Poisson noise from the source and sky background, which should be relatively consistent since the exposure time and other observational parameters are fixed for all targets (∼26 AB; $t_{\mathrm{exp}} \sim 400$ s; Table 4 in J. C. Lee et al. 2023). In F335M, the galaxy background is dominated by diffuse PAH emission and the unresolved light from stars. As expected, the F335M detection limit correlates with the galaxy's star formation rate (SFR; Table 1 in J. C. Lee et al. 2022). In Section 5.2, the F335M images of the galaxy sample make clear the substantial range in galaxy surface brightness, corresponding to the lowest F335M detection limit for IC 5332 and the highest in NGC 3627.

Our selection of compact PAH sources is primarily based on the dispersion of the F300M − F335M color as a function of magnitude for continuum sources (the red and yellow curves in Figure 2). These color dispersion curves should be computed for the specific imaging observations of interest. However, a simple way of characterizing our color selection curves to provide a point of comparison for other studies is to calculate the value of the 5σ dispersion at F335M = 20 for each galaxy. The median value corresponds to F300M − F335M = 0.67, with a range of 0.35–0.84.

4.2. Exclusion of Old Objects

Our sample of 3.3 μm PAH emitters may encompass a variety of objects, among which are evolved stars that have undergone significant mass loss (e.g., F. Galliano et al. 2008), resulting in high optical obscuration and pronounced brightness in the near and mid-IR due to the circumstellar envelopes. These objects include carbon-rich AGB stars (e.g., M. A. T. Groenewegen 2022) and PNe (e.g., R. Ohsawa et al. 2013). As the primary focus of this work is on young dusty objects, we wish to remove these older objects from our compact 3.3 μm PAH sample.

Star-forming regions contain a larger amount of cooler dust, while the high optical depth dust surrounding AGB stars is warmer. As a result, young dusty objects should exhibit a rising SED in the mid-IR, and the ratio $F_\nu(\mathrm{F2100W})/F_\nu(\mathrm{F1000W}) > 1$ should be larger than 1. A conservative choice of removing sources with $F_\nu(\mathrm{F2100W})/F_\nu(\mathrm{F1000W}) < 3$ is justified in Appendix A. The ∼2 times broader PSF at F2100W compared to F1000W increases $F_\nu(\mathrm{F2100W})/F_\nu(\mathrm{F1000W})$, so we may retain some evolved stars in confused regions, but this color cut ensures that no bona fide young clusters are mistakenly removed.

We also apply criteria to remove objects from the sample whose F300M − F335M color may reflect a rising near-IR SED rather than PAH emission and limit the sample to sources with $F_\nu(\mathrm{F360M})/F_\nu(\mathrm{F335M}) < 1$.

We compare the 10 μm and 21 μm properties of our final cleaned selection of 3.3 μm PAH emitters with the sample from O. C. Jones et al. (2017), which includes more than 1000 point sources in the Large Magellanic Cloud (LMC) observed with the Spitzer IRS and reduced by the SAGE-Spec Spitzer legacy program (F. Kemper et al. 2010). O. C. Jones et al. (2017) derived synthetic MIRI photometry for this sample, which encompasses various types of objects, including young stellar objects (YSOs), H II regions, main-sequence stars, AGB stars, post-AGB stars, and PNe.

Figure 3 shows the F1000W versus F1000W − F2100W CMD (similar to Figure 3(c) of O. C. Jones et al. 2017), where in each panel we place the SAGE LMC sample at the distance of the parent galaxy, to compare the distributions of the various populations with our final selection of PAH emitters (Figure 3). We show the PNe and all the different stellar objects from O. C. Jones et al. (2017) under the "star" category and combine all the types of YSOs+H II regions into the "YSO and H II regions" category. We also plot a PHANGS-HST candidate sample of red evolved stars (Appendix A) for galaxies at distances less than 10 Mpc (first row of panels only), where individual red old stars may still dominate the light subtended by the 10 μm and 21 μm PSF (0.″328 and 0.″674 FWHM, respectively).

The vertical line in these plots corresponds to the adopted limit of $F_\nu(\mathrm{F2100W})/F_\nu(\mathrm{F1000W}) = 3$ (or F1000W − F2100W = 1.2 AB mag). We observe from these plots that this adopted value helps to separate the O. C. Jones et al. (2017) LMC sample of stars from YSOs+H II regions (both populations shown as contours in Figure 3). While PAH emitters generally exhibit similar F1000W − F2100W colors but brighter F1000W magnitudes compared to YSOs+H II regions, there is some overlap between these populations in the closest galaxies. This suggests that the physical resolution and depth in NGC 5068 and IC 5332 allow the detection of compact clusters dominated by a single massive YSO as well as individual H II regions, a topic we discuss further in Section 4.4.

We also observe that PNe are very faint in F1000W, much below the point-source detection limit in the emptiest areas of

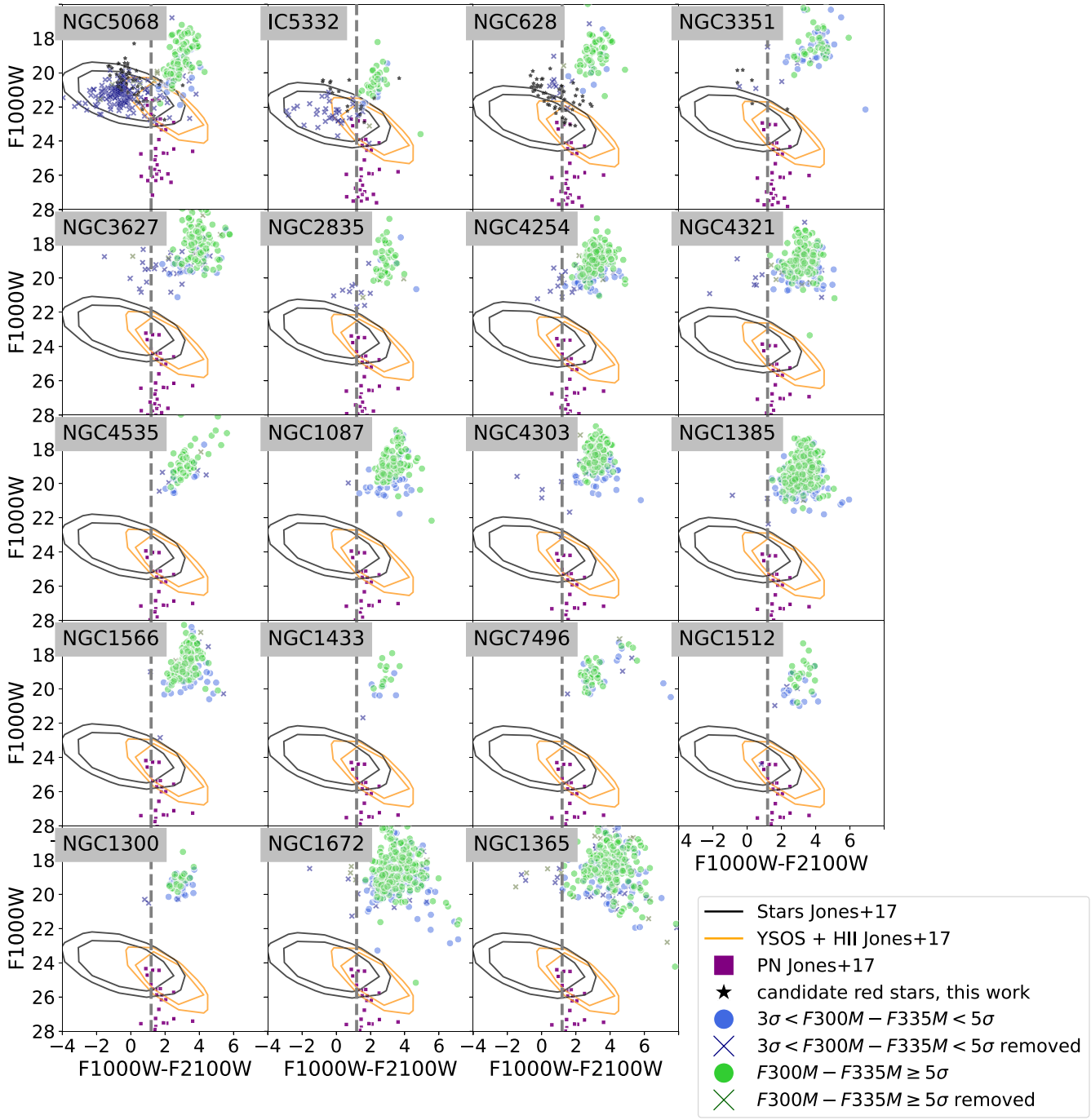

Figure 3. F1000W vs. F1000W − F2100W CMDs showing the compact 3.3 μm PAH emitters (green and blue points) from this analysis and a comparison sample from O. C. Jones et al. (2017) that includes pointlike sources in the LMC: PNe (purple points), YSOs and H II regions (orange contours), and different kind of stars (black contours representing 98th and 99.9th percentiles). Objects that were removed from our 3.3 μm PAH emitter sample are shown with crosses. Our sample of red evolved stars (see Appendix A) is shown with black points for galaxies at distances <10 Mpc. The vertical line at F1000W − F2100W = 1.2 mag ($F_{21\ \mu m}/F_{10\ \mu m} = 3$) corresponds to the adopted limit (see text for details). As in all the plots, galaxies are sorted by distance. The fact that the angular resolution scales with wavelength for both the JWST and Spitzer (O. C. Jones et al. 2017) data points should be kept in mind when interpreting this plot.

the images (∼23 AB; J. C. Lee et al. 2023, Table 4). Therefore, contamination from these objects is unlikely. We also conducted a visual inspection of the images to identify potential background galaxies within our sample. However, no clear contaminants of this type were observed.

4.3. The 3.3 μm PAH Young Cluster Candidate Sample

After applying the F_ν(F360M)/F_νF335M < 1 and F_ν(F2100W)/F_ν(1000W) = 3 conditions to remove contaminants, we keep a total of 1816 compact objects detected above the 5σ color dispersion across the 19 galaxies; this is 88% of the original color–magnitude selected sample. Table 3 lists the number of compact 3.3 μm PAH emitters likely associated with young dusty stellar populations in each galaxy.

Figure 4 shows the number of PAH emitters against the total galaxy SFR and the integrated CO (2–1) luminosity L_{CO} from J. C. Lee et al. (2023). As expected, the number of PAH emitters generally increases with both the SFR and L_{CO},

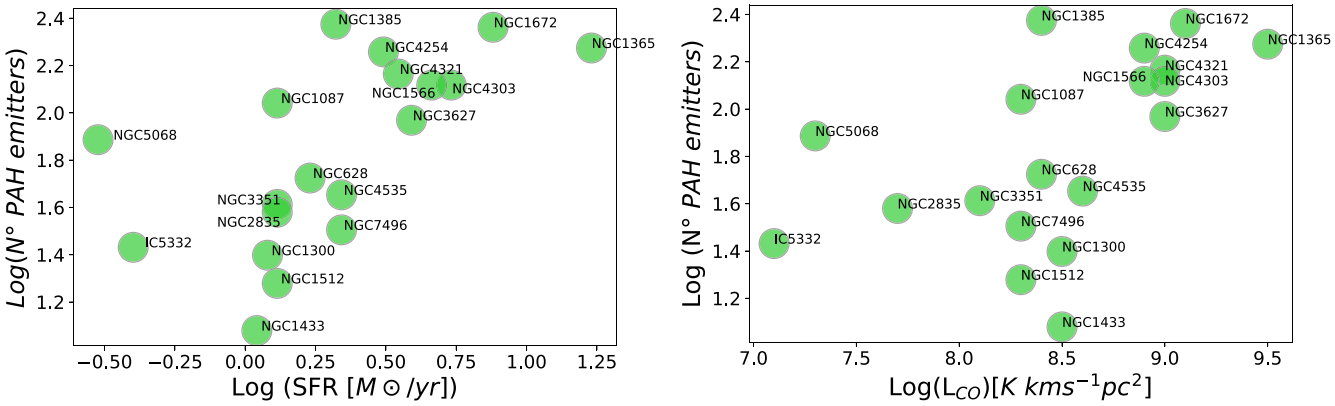

Figure 4. Number of PAH emitters detected above the 5σ color dispersion (see Sections 4.1 and 4.2) against the total galaxy SFR (left) and the integrated CO (2–1) luminosity (L_{CO}; right). Values for SFR and L_{CO} are from J. C. Lee et al. (2023, Table 2). The number of compact PAHs correlates with the SFR and L_{CO}, as would be expected.

Table 3
Counts of PAH Emitters and HST Clusters

Galaxy	PAH Emitters		HST Cls. ⩽ 3 Myr		HST-PAH		⩽3 Myr		4–5 Myr		6–10 Myr		11–1000 Myr	
	3σ–5σ	>5σ	H	ML	H	ML	H	ML	H	ML	H	ML	H	ML
(1)	(2)	(3)	(4)	(5)	(6)	(7)	(8)	(9)	(10)	(11)	(12)	(13)	(14)	(15)
NGC 5068	18	77	27	35	12	11	15/27	15/35	1/2	0/2	0/8	0/15	0/44	0/67
IC 5332	8	27	11	15	9	10	10/11	14/15	…	…	0/9	0/7	0/18	0/13
NGC 628	10	53	44	55	9	11	11/44	14/55	0/2	0/2	0/23	0/35	0/31	0/40
NGC 3351	31	41	17	15	0	0	2/17	1/15	4/17	3/16	0/10	0/9	1/5	1/6
NGC 3627	20	93	18	12	2	2	4/18	4/12	2/20	2/16	0/11	0/12	0/63	0/66
NGC 2835	4	38	14	13	6	7	6/14	7/13	…	…	0/13	0/5	0/28	0/23
NGC 4254	60	181	64	72	9	12	13/64	19/72	3/17	4/21	0/45	0/57	0/76	0/110
NGC 4321	61	146	71	59	7	8	10/71	11/59	5/36	5/30	0/30	0/30	2/58	2/48
NGC 4535	11	45	23	18	5	3	8/23	7/18	2/8	1/7	0/10	0/6	1/26	1/23
NGC 1087	39	110	36	30	11	10	16/36	17/30	1/5	1/6	0/19	0/18	0/45	0/41
NGC 4303	47	131	68	71	19	25	28/68	31/71	0/11	0/11	0/39	0/38	0/100	0/113
NGC 1385	111	237	59	43	12	12	18/59	15/43	1/9	1/6	0/23	0/14	1/101	1/97
NGC 1566	35	131	38	31	11	13	17/38	19/31	1/2	1/1	0/31	0/30	0/51	1/52
NGC 1433	6	12	6	6	2	3	2/6	3/6	0/2	0/2	2/7	2/6	0/4	1/4
NGC 7496	18	32	20	18	5	8	6/20	9/18	0/4	0/5	0/7	0/6	0/15	0/16
NGC 1512	15	19	16	10	2	2	2/16	2/10	1/8	1/4	0/5	0/11	1/14	0/10
NGC 1300	23	25	18	24	4	5	5/18	6/24	1/3	1/1	0/7	0/24	0/12	0/17
NGC 1672	119	230	43	48	9	14	13/43	18/48	3/29	3/26	0/20	0/27	1/65	1/84
NGC 1365	87	188	31	28	2	1	5/31	4/28	8/61	7/44	0/10	0/6	2/99	1/93
Sum.	723	1816	624	603	136	157	191/624	216/603	33/236	30/200	2/327	2/356	9/855	9/923
Min.	4	12	6	6	0	0	0.12	0.07	0	0	0	0	0	0
Max.	119	237	71	72	19	25	0.91	0.93	0.5	1	0.29	0.33	0.2	0.25
Median	23	77	27	28	7	8	0.3	0.38	0.12	0.14	0	0	0	0

Note. Columns (2) and (3): number of PAH emitters with $3\sigma \leqslant$ F300M − F335M $< 5\sigma$ (2) and F300M − F335 $\geqslant 5\sigma$ (3). Columns (4) and (5): number of HST clusters from D. Maschmann et al. (2024) and D. Thilker et al. (2024) younger than 3 Myr and brighter than our established detection threshold in F300M and F335M in HST class 1 and 2 human (4) and machine learning (5). Columns (6) and (7): number of HST clusters younger than 3 Myr that are also found in the F300M − F335M $\geqslant 5\sigma$ PAH emitter sample. Columns (8) and (9): fraction of HST clusters ⩽3 Myr with F300M − F335M $\geqslant 3\sigma$. Columns (10) and (11): fraction of HST clusters between 4 and 5 Myr with F300M − F335M $\geqslant 3\sigma$. Columns (12) and (13): fraction of HST clusters between 6 and 10 Myr with F300M − F335M $\geqslant 3\sigma$. Columns (14) and (15): fraction of HST clusters between 11 and 1000 Myr with F300M − F335M $> 3\sigma$.

highlighting that the number of compact PAH emitters should scale with the star formation activity and gas supply of the galaxy. The sample size spans from 12 to 237 (NGC 1433–NGC 1385), with a median of 77. These sample sizes will be discussed later in the work in relation to the number of optically detected young clusters as reported in the PHANGS-HST star cluster catalog (D. Maschmann et al. 2024).

Figure 5 presents examples of the detected compact PAH emitters across the 14 observed bands from HST UV to JWST 21 μm. These objects are located in a northern region of the galaxy NGC 3627 (see right panel). Some objects are undetected or very faint in the HST bands (objects 2, 3, and 4), while others, despite not being detected or being very faint in the HST broad bands, appear clearly in the HST Hα narrow

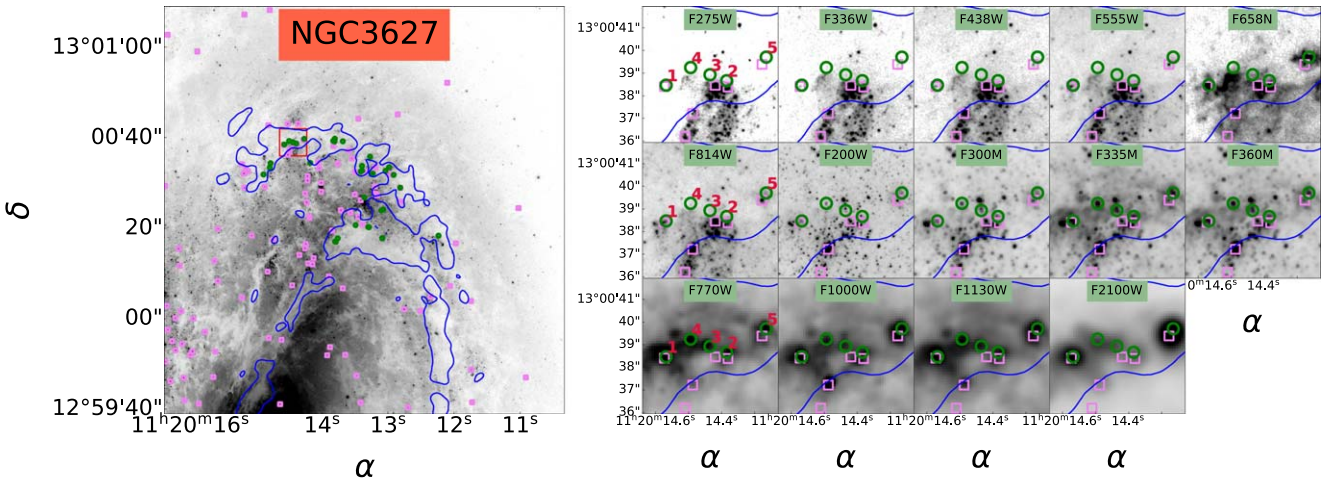

Figure 5. Example of compact 3.3 μm PAH emitters (green) detected in a northern region of the galaxy NGC 3627, located at a distance of 11.32 Mpc. The left panel shows an HST F555W image of the northern part of the galaxy, with the red box indicating the region displayed in the zoomed-in view on the right, across the 14 observed bands. The sample includes objects that are completely undetected in the HST broad bands (objects 2, 3, and 4), others that are undetected or very faint in the HST broad bands but appear very bright in the Hα narrow band (object 5), and objects that are visible in all or almost all of the HST broad bands (object 1). PHANGS-HST clusters from D. Maschmann et al. (2024) younger than 10 Myr are shown with pink squares, and ALMA CO(2–1) intensity contours are shown in blue. We will discuss the spatial distribution of PAH emitters in relation to both the CO contours and HST clusters in Section 6.3.

band (object 5). Other objects in our sample, such as object 1 in this example, are detected in the HST broad bands. All these objects show increasing brightness observed in the near-IR and mid-IR bands. We will discuss these different categories in Section 7.1. Figure 6 shows the observed SED for these five objects. Objects not detected in HST broad bands are shown with upper limits. The flux densities corresponding to the MIRI bands are also shown as crosses, since we adopted apertures covering larger physical scales than those used for the HST and NIRCam bands (due to the lower MIRI resolution; Table 1). We can distinguish the emission features at Hα and 3.3 μm, as well as an apparent dip at 10 μm compared to the neighboring 7.7 and 11.3 μm filters. This spectral shape likely results from strong PAH emission at 7.7 μm and 11.3 μm that does not significantly contribute to F1000W. It is possible that some objects may have true silicate absorption at 10 μm. However, the 9.7 μm silicate absorption optical depth is $\sim 1/10\ A_V$ (G. H. Rieke & M. J. Lebofsky 1985; V. Ossenkopf & T. Henning 1994; B. T. Draine & B. S. Hensley 2021). Absorption is sometimes seen in the spectra of individual YSOs at high resolution (e.g., F. Kemper et al. 2010) and toward AGN (H. W. W. Spoon et al. 2000), but it is unlikely to be common in these star formation regions observed with larger apertures. Follow-up mid-IR spectroscopy will be required to establish whether the F1000W point in these objects actually represents silicate absorption or is simply the dust continuum in between the PAH features.

4.4. Possible Detection of Individual Massive YSOs and OB Stars in the Nearest Galaxies

Careful examination of the CMD for NGC 5068 and IC 5332 (first two panels in Figure 2) reveals an additional population that manifests as a knobby overdensity, generally located between the 3σ and 5σ curves, i.e., in the region of $0.5 \lesssim \mathrm{F335M} - \mathrm{F300M} \lesssim 1$, and a limited range of magnitudes, $21 \lesssim \mathrm{F335M} \lesssim 23$ in NGC 5068 and $22.5 \lesssim \mathrm{F335M} \lesssim 24.5$ in IC 5332. One can even make out signs of such a population in NGC 0628, although it is fainter and blends into the noise.

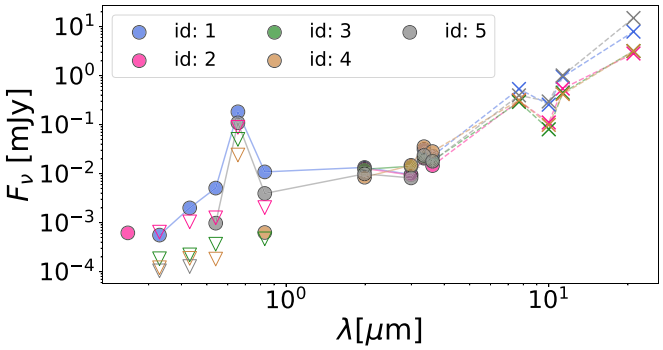

Figure 6. Observed SED for the five objects shown in Figure 5. Upper limits indicated by open downward-pointing triangles are presented for objects that are not detected in the HST bands. For MIRI band detections, upper limits are shown by crosses. In this case there is a detection, but due to the coarser resolution of MIRI, the resulting fluxes correspond to a larger physical scale than those shown for the HST and NIRCam bands.

To investigate further, we examined the Milky Way ISO H II region sample described in E. Peeters et al. (2002), using the high-level data products retrieved from the ISO archive. The sources are a few to 10 pc in size and have bolometric luminosities of a few $\times\ 10^4$ to a few $\times\ 10^6\ L_\odot$ and ionizing photon luminosities measured from a centimeter continuum of 10^{47} to a few $\times\ 10^{50}$ photons s^{-1}—exactly what is expected for one or a few OB stars still associated with their nascent gas (F. Martins et al. 2005). We convolved the spectra with JWST filter profiles to synthesize F335M and F300M fluxes and find that these Milky Way ISO H II regions have an F335M – F300M color of 0.5–1 mag and, at the distances of NGC 5068 and IC 5332, F335M magnitudes consistent with the location of the knobby overdensity of 3σ–5σ PAH sources. The nature of this population in the most nearby galaxies will be further investigated in future work, but the properties are consistent with the detection of individual OB stars (or clusters with a handful of them) beginning to clear their natal material.

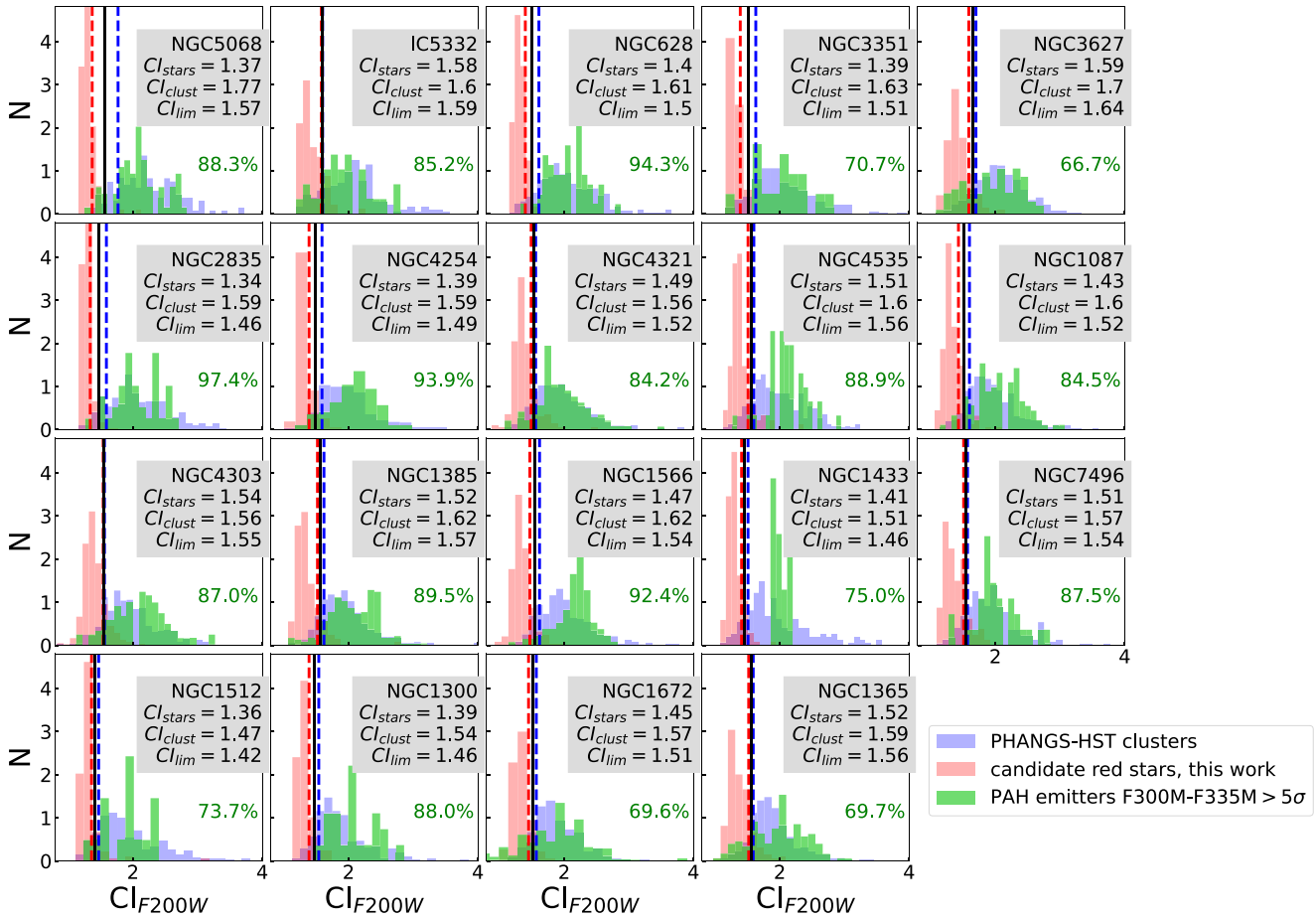

Figure 7. F200W CI—difference between F200W photometry measured in circular apertures with radii of 1 and 4 pixels—distribution for PHANGS-HST class 1 and 2 star clusters (blue), candidate red evolved stars (red), and $>5\sigma$ PAH emitters (green). The red dashed line indicates the 84% quantile of the candidate red stars, denoted as CI_{stars} in the top right corner of each plot. The blue dashed line corresponds to the 16% quantile of the cluster population, and its value is indicated as CI_{clust}. The black solid line indicates the mean value between these two quantiles, indicated as CI_{lim}, which can be used to distinguish cluster-dominated and point-source/star-dominated samples. Each panel includes in green the percentage of PAH emitters with CI values consistent with star clusters, which varies across galaxies with a median of ∼70%. The plots are organized by increasing galaxy distance from the upper left corner to the bottom right. Histograms are normalized by the total number of objects and the width of the bin.

5. Properties of 3.3 μm PAH Emitters

5.1. CI Analysis

To investigate the nature of the 3.3 μm PAH emitters and assess the likelihood that they are star clusters, we conducted a CI analysis. The CI serves as a metric to quantify the degree of central concentration in the light distribution of an object, providing an indication of its compactness. This method has been widely employed in various HST studies of star clusters in nearby galaxies to differentiate them from individual stars (e.g., R. Chandar et al. 2010; B. C. Whitmore et al. 2014a; D. O. Cook et al. 2019; S. Deger et al. 2022). In B. C. Whitmore et al. (2023), published as part of the ApJL PHANGS-JWST First Results Issue, we found that a CI computed from JWST F200W imaging for NGC 1365 improves the distinction between stars and clusters compared with CI computed from HST F814W imaging. The CI for star clusters in nearby galaxies is computed as the difference in photometry measured using circular apertures. B. C. Whitmore et al. (2023) adopt radii of 1 and 4 pixels for the JWST F200W imaging and 1 and 3 pixels for the HST F814W imaging. The outer radii both subtend $0\farcs12$, given the smaller PSF of the NIRCam short-wavelength detectors compared with HST WFC3 UVIS (pixel scales are $0\farcs03$ versus $0\farcs04$, respectively). Based on this definition, we found that a value of CI = 1.4, based on JWST F200W imaging, was determined to be a good threshold between point-source/star-dominated and cluster-dominated populations in that one galaxy.

Now expanding the analysis to all galaxies, we computed CI_{F200W} for all clusters in the PHANGS-HST cluster catalogs (D. Maschmann et al. 2024) and for red evolved star candidates (selected as explained in Appendix A). Aperture photometry for these small apertures was conducted using a fractional pixel method to determine the overlap of the aperture on the pixel grid. In Figure 7, we present the distribution of CI values for the red evolved star candidates (red), HST star clusters (blue), and $>5\sigma$ PAH emitters (green) for each galaxy. The red dashed line indicates the 84% quantile of the red evolved star candidates, the blue dashed line indicates the 16% quantile of the HST cluster population, and the black solid line indicates the mean between these two values. We adopt the mean value to distinguish between stars and clusters. These three CI values are also indicated in the top corner of each panel in Figure 7 and are slightly larger than (∼10%) but generally consistent with the value of 1.4 reported in B. C. Whitmore et al. (2023). As expected, it becomes more difficult to distinguish clusters

from point sources as the distance of the parent galaxy increases from 5 Mpc to 20 Mpc. At 10 Mpc, the F200W PSF (FWHM 0.″066) subtends 3.2 pc, and the 1 pixel and 4 pixel radii used to compute CI subtend 1.5 pc and 6 pc. Star clusters typically have half-light radii of a few parsecs (S. F. Portegies Zwart et al. 2010; J. E. Ryon et al. 2017; M. R. Krumholz et al. 2019; G. Brown & O. Y. Gnedin 2021).

To the left of the vertical black line, we find the most compact objects with CI values typically associated with stars, while to the right, we find slightly more extended objects that exhibit CI values consistent with star clusters. The figure provides the percentage of PAH emitters located on the right side of each panel, indicating those within the cluster regime.

The percentage of objects in the star cluster CI regime varies from galaxy to galaxy and ranges from 66% to 97% with a median of 87%. The percentage does not show a correlation with galaxy distance, but recall that many of the sources that are potentially individual evolved red stars shown in the histograms in Figure 7 are removed from the PAH emitter sample in the closer galaxies by the F1000W − F2100W color cut imposed in Section 4.2.

PAH emitters with smaller CI than the values indicated by this limit (black line) do not necessarily imply their exclusion as clusters. As depicted in Figure 7, there remains a tail in the cluster population with small CI values, suggesting the possibility of very compact star clusters or clusters dominated by a single massive YSO, which are also interesting for our analysis. Moreover, younger clusters are also expected to be more compact, as clusters should expand as they age due to mass loss and two-body relaxation (G. Brown & O. Y. Gnedin 2021 and references therein). For these reasons, we opt to keep the objects with small CI (again, which already have been filtered for possible old red stars) in the sample.

A key question is how source crowding will affect the F200W CI values presented here. This is particularly important for deep, highly resolved imaging at 2 μm, which will be far more sensitive to the large population of older stars compared with HST optical imaging. This issue can be investigated in future work, for example, when PSF fitting catalogs have been produced for our F200W imaging.

5.2. Spatial Distribution

The PHANGS-JWST Cycle 1 galaxy sample provides an excellent opportunity to study the locations of compact PAH emitters within galaxies, given its inclusion of a diverse range of galaxy morphologies and masses. Figure 8 overlays the PAH emitter population on the detection image (F335M) for each galaxy. The PAH emitters are generally found in the spiral arms of the galaxies or concentrated on the bar ends. They also delineate outer and inner star-forming rings such as in NGC 3351, NGC 4321, and NGC 1672. The figures provide assurance that the adopted selection criteria yield samples that are not merely capturing diffuse PAH emission but are instead tracing compact regions of star formation. It is interesting to note that in almost all galaxies, the bar is free of PAH emitters, with three exceptions, in the bars of NGC 5068, NGC 1087, and NGC 1385. Interestingly, these galaxies also exhibit a more flocculent morphology and are the lower-mass galaxies in the sample (Table 2 of J. C. Lee et al. 2023). The environment here may not be as turbulent as in galaxies with clearly defined spiral arms, potentially influencing the facilitation of star formation.

Figure 9 shows the distribution of PAH emitters but this time focusing on just two galaxies, NGC 3627 and NGC 4321, to illustrate the location of the PAH emitters relative to dust, which is apparent as attenuation features in the HST F555W image. The PAH emitters are primarily located in the dust lanes within the spiral arms of these galaxies. While we only show these two cases, this is observed in most galaxies. These images also present the distribution of the 5σ (green) and 3σ–5σ (blue) PAH emitter selections, showing that they exhibit similar spatial distributions.

5.3. 3.3 μm PAH Luminosities

Another basic property of the emitters is their 3.3 μm PAH luminosity. To compute the 3.3 μm PAH emission flux, we use the flux density obtained from the F300M photometry to estimate the contribution from the continuum to the F335M band. We decided to use only F300M for the estimation of the continuum instead of a combination of the F300M and F360M bands, as F360M is contaminated by PAH emission (K. M. Sandstrom et al. 2023). The median 3.3 μm PAH luminosity of the aggregate sample across all 19 galaxies is 3.5×10^{35} erg s^{-1} with a range of 2.5×10^{34} (IC 5332) to 1.5×10^{37} (NGC 1365) erg s^{-1}.

To put these values into context, we estimate the luminosity of 30 Doradus (aka the Tarantula Nebula) based on its integrated flux in the 6.2 μm feature of 2.5×10^{-14} W m^{-2} (F. Galliano et al. 2008). This number is fairly uncertain since the feature-to-continuum ratio is very low in 30 Doradus, and the emission is not compact; we have chosen the "peak" number, but there is extended emission nearly an order of magnitude brighter around the peak. We choose the 6.2 μm feature because theory suggests that the 3.3/6.2 ratio (0.3–0.9) is less sensitive to PAH size than other ratios, with the majority of the energy of both of these short-wavelength features being emitted by smaller PAHs (A. Maragkoudakis et al. 2023). This results in an estimated compact 3.3 μm luminosity of 5×10^{36} erg s^{-1}. Although this value is higher than the median luminosity across the entire sample of galaxies presented here, it falls within the overall luminosity range. The central young star cluster associated with 30 Doradus, NGC 2070, is relatively uncommon in nearby galaxies; it has a large number of young massive ionizing stars and a large overall stellar mass ($\sim 10^5$ $M_\odot$; B. Brandl et al. 1996; R. Domínguez et al. 2023), which is significantly more massive than the cluster population in the PHANGS-HST galaxies (median of $\sim 10^4$ $M_\odot$). We found higher luminosities than this value just in two galaxies or our sample NGC 1672 and NGC 1365. Consistently, these galaxies also present the highest SFR and L_{CO} (Figure 4).

5.4. Stellar Mass Estimates

To estimate the stellar masses of the PAH emitters, we use a mass-to-light ratio derived in F200W for the HST clusters from D. Maschmann et al. (2024) and D. Thilker et al. (2024) with ages $\leqslant$3 Myr. If the PAH emitters are subject to larger amounts of dust attenuation than the optically detected clusters, then the computed masses will underestimate the true stellar mass; nevertheless, they should be useful as an estimate for a first examination of the properties of the sample.

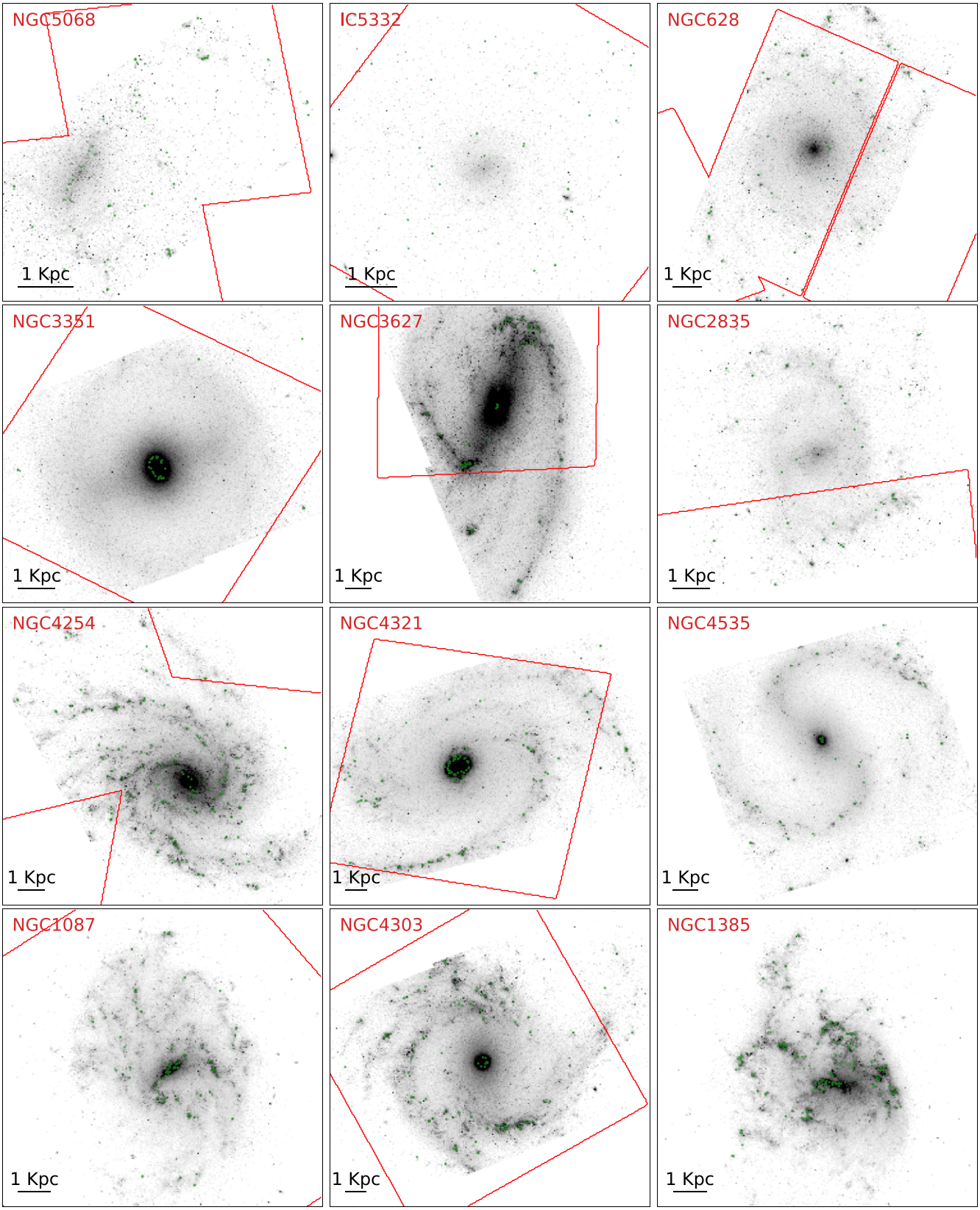

Figure 8. Spatial distribution of the $<5\sigma$ PAH emitters overlaid in a JWST F335M image of the galaxies. The plots are organized by increasing galactic distance from the upper left corner to the bottom right. The red footprints shows the HST Hα observations.

To determine the mass-to-light ratio, we fit a line to the F200W absolute magnitude $M_{\rm F200W}$ as a function of the logarithm of cluster stellar mass, where the cluster stellar masses are computed via SED fitting with HST photometry as in D. Thilker et al. (2024; a brief overview is provided in the next section). We derived the following relation: $M_{\rm F200W} = -2.55 \pm 0.03 \quad \log(M/M_{\odot}) + 2.48 \pm 0.15$ (Figure 10). We applied this relationship to our list of PAH emitters and

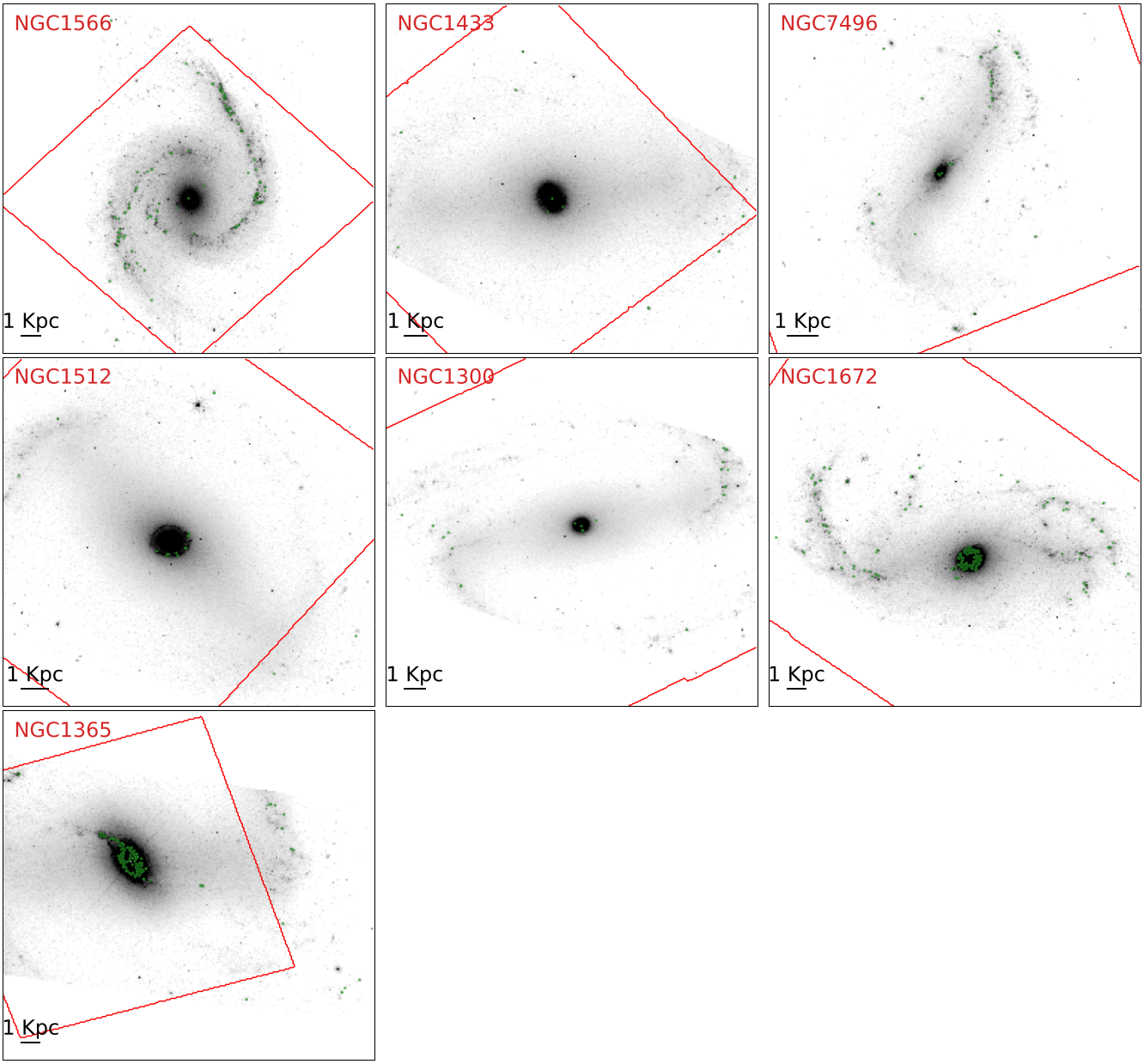

Figure 8. (Continued.)

obtained masses in the range 700 $M_\odot$ (NGC 5068) to 6.5×10^5 $M_\odot$ (NGC 1365), with a median of 3.4×10^4 $M_\odot$. The obtained mass distribution is presented in Section 6.1.

6. Comparison with PHANGS-HST Cluster Catalogs

6.1. HST Star Clusters on the F300M − F335M CMD

Here, we examine the 3.3 μm PAH properties of optically detected star clusters in the PHANGS-HST catalogs (D. Maschmann et al. 2024). The goal is to use the star cluster ages to gain insight into the duration of compact PAH emission associated with young stellar populations. The HST star cluster ages adopted in this analysis are taken from D. Thilker et al. (2024) and computed through SED fitting of NUV-*U*-*B*-*V*-*I* HST photometry with priors on model age, reddening, and metallicity determined from ground-based Hα imaging and other observable parameters providing categorical insight (morphology, color–color information). The JWST photometry follows the same procedure as described in Section 3.2 with apertures centered on the position of each optical cluster. PHANGS-HST provides two types of catalogs: catalogs in which a subset of cluster candidates have been visually inspected and morphologically classified by a human and catalogs where all candidates have been classified by neural networks. The latter, which we refer to as the machine learning catalogs, are on average $\sim$1 mag deeper than the human-classified catalogs. In the following analysis, we examine clusters classified as class 1 (single-peak and symmetric) and class 2 (single-peak and elongated or asymmetric) in both human-classified and machine learning catalogs.

Two sets of F335M versus F300M − F335M CMDs are presented that overlay the HST clusters in different age

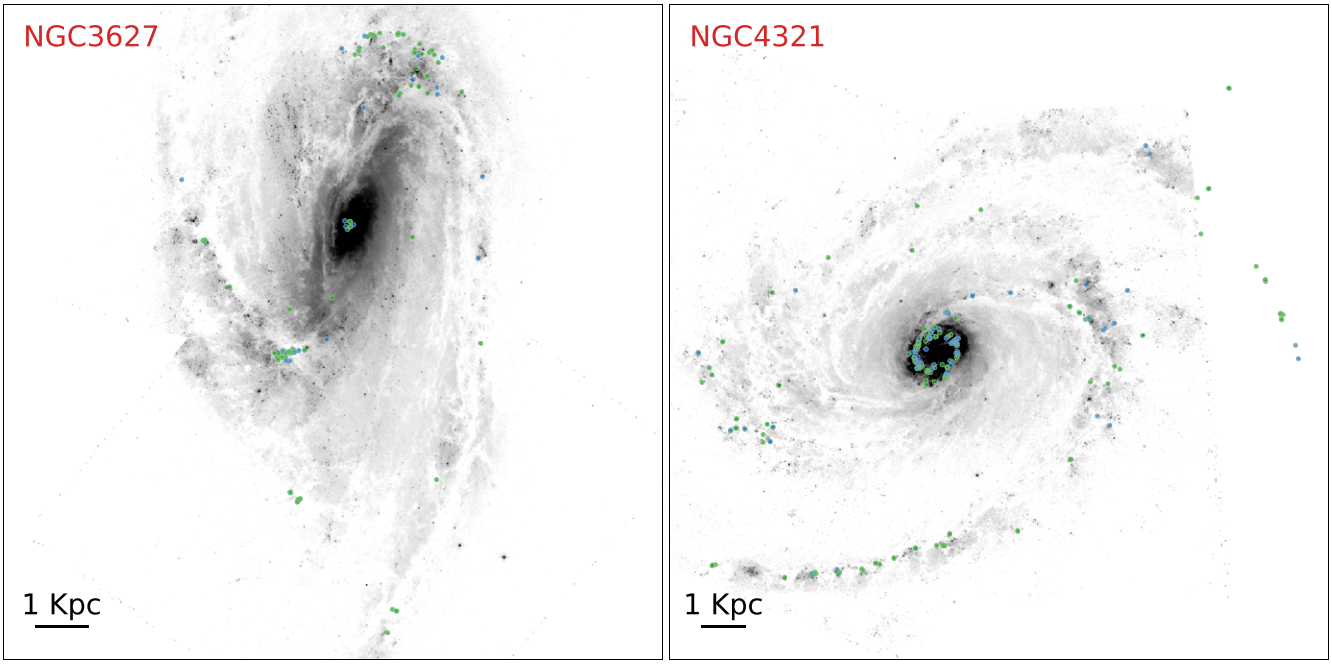

Figure 9. Spatial distribution of PAH emitters in NGC 3627 and NGC 4321 overlaid on the HST F555W image of the galaxies. We observe that the PAH emitters are mainly located in and around the dust lanes. Here we show both 5σ (green) and 3–5σ PAH (blue) samples.

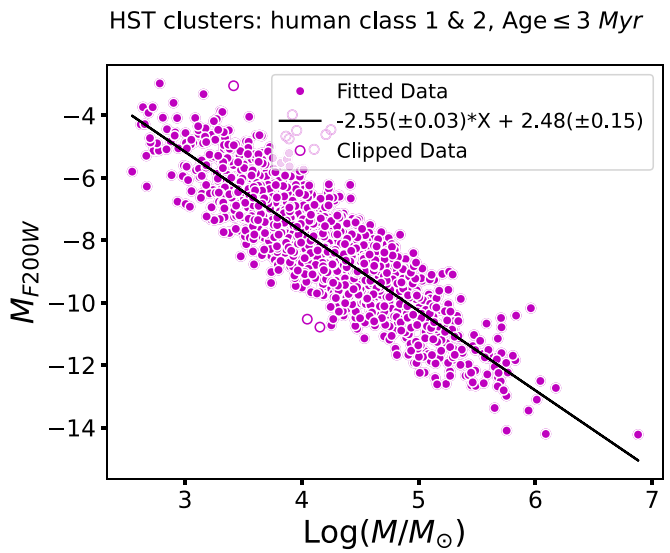

Figure 10. Mass-to-light ratio in the F200W band for the HST cluster catalog class 1 and 2 with ages $\leqslant$3 Myr. The relation derived here was used to estimate the masses of the PAH emitters.

ranges on the F335M detections for each galaxy as initially presented in Figure 2. Figures 11 and 12 show young clusters with ages of $\leqslant$3 Myr and 4–10 Myr, respectively. The specific number of HST clusters in different age bins in each galaxy whose colors fall in the F300M − F335M PAH-excess selection region ($>3\sigma$) over the total number of HST clusters above the F300M and F335M detection limit threshold are listed in Table 3.

Depending on the galaxy, between 12% and 93% (with a median of ∼30%) of clusters $\leqslant$3 Myr fall within the PAH emitter region of the F300M − F335M color–magnitude space, i.e., with a color excess larger than 3σ (red curve in the CMDs of Figures 11 and 12). By contrast, only ∼13% of HST clusters with 4–5 Myr ages fall within the PAH emitter region (Figure 12 and Table 3), and very few clusters older than this present F300M − F335M $> 3\sigma$. It is intriguing that so many clusters younger than 3 Myr do not show significant PAH feature emission, i.e., F300M − F335M near zero. This may be due to the selection effects inherent in the HST cluster catalog, namely, that clusters detected in blue or even UV filters are not heavily extinguished and thus may be associated with a lower-than-average circumstellar medium and ISM. Other likely effects are inaccurate age dating (the HST clusters are in fact older) or, more interesting if true, strong feedback clearing or destroying the PAHs in these clusters. Nevertheless, the number of HST clusters that *do* show strong PAH emission visibly decreases with cluster age, and the timescale for clusters to lose that PAH excess emission is clearly less than 5 Myr. In the last two columns of Table 3, we can see that the numbers of HST clusters older than 10 Myr with significant F300M − F335M color excess is almost zero, indicating an increasing lack of PAH emission with cluster age, and that very few if any clusters retain strong PAH emission at ages beyond a few Myr.

In Figure 13, we present the age histograms of all HST clusters whose F300M and F335M photometry lies in the $>3\sigma$ PAH emitter region. This demonstrates again that most of the PAH-emitting clusters are younger than 10 Myr, with the exception of a very few clusters. We inspected the oldest objects across the 14 bands, and their brightness and morphologies in the Hα, F335M, and mid-IR bands lead us to believe that they are likely very young clusters with inaccurately estimated ages via UV-optical SED fitting.

We note that accurate age dating is difficult in the 5–10 Myr age range (optical stellar colors change rapidly as red

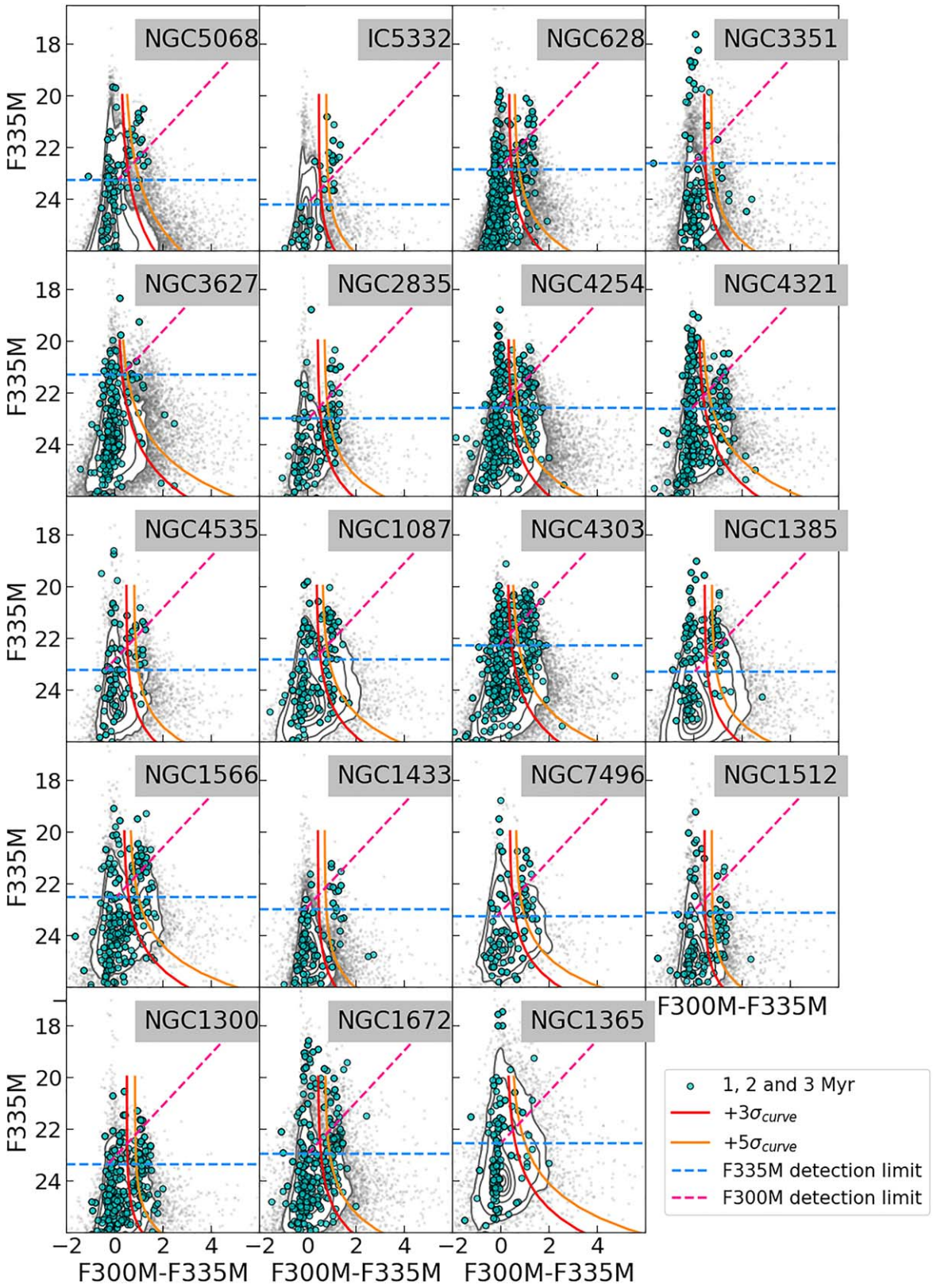

Figure 11. F335M vs. F300M − F335M CMDs. The contours represent the 5th, 10th, 30th, 50th, 70th, and 90th density percentiles of all the sources detected over the F335M images (see Section 3.1). The small gray dots indicate regions where the density is lower than the 5th percentile. Cyan circles are PHANGS-HST clusters with ages of 1, 2, and 3 Myr. The red and orange curves indicate $+3\sigma$ and $+5\sigma$ in color dispersion, respectively. The dashed horizontal lines indicate the adopted F335M (light blue) and F300M (pink) detection limits for the PAH emitter sample, derived from 5σ measurements relative to the mean obtained via random apertures (see Section 4.1). The plots are organized by the galaxies' increasing distance from the upper left corner to the bottom right.

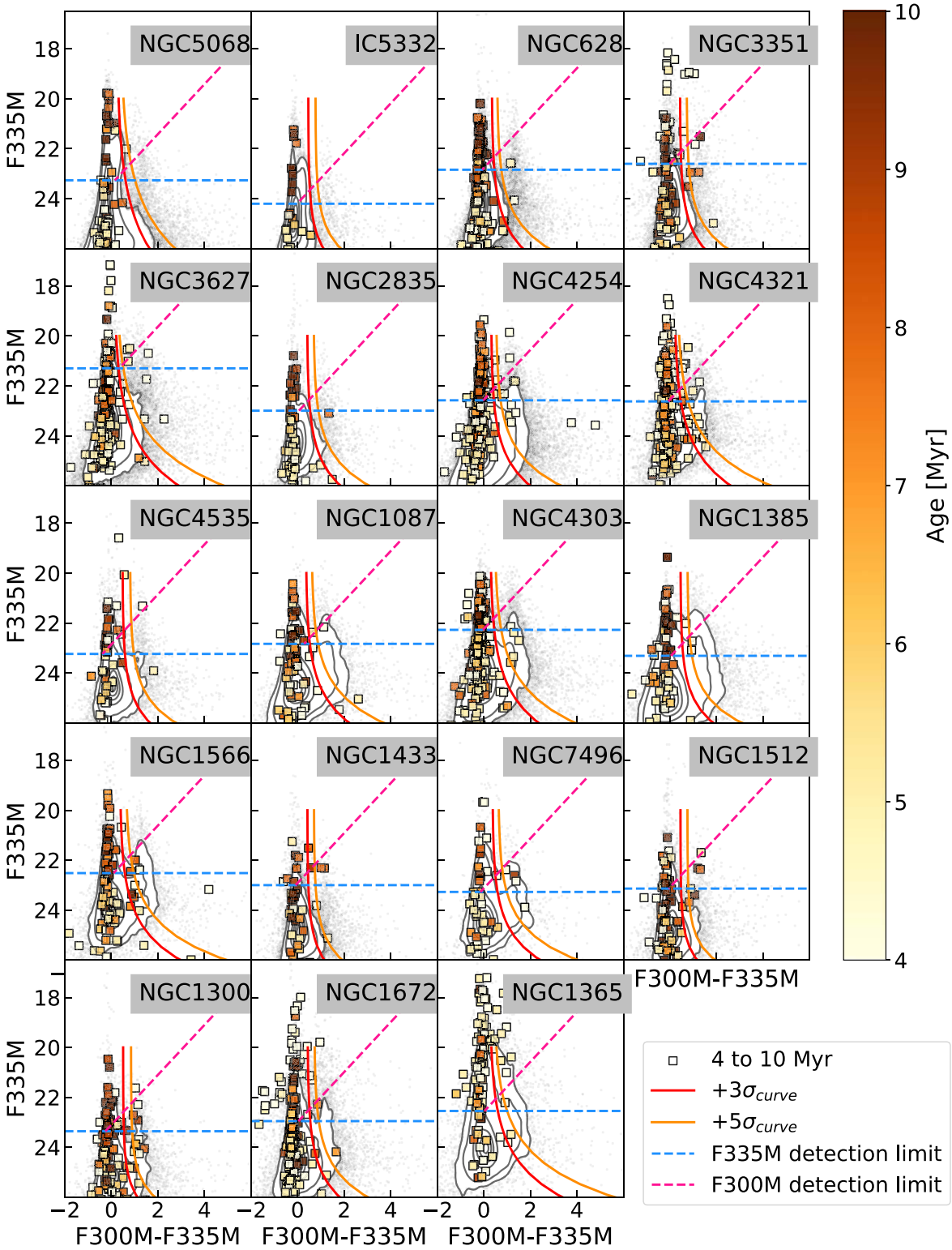

Figure 12. F335M vs. F300M − F335M CMDs. The contours represent the 5th, 10th, 30th, 50th, 70th, and 90th density percentiles of all the sources detected over the F335M images (see Section 3.1). The small gray dots indicate regions where the density is lower than the 5th percentile. The colored squares represent PHANGS-HST clusters aged 3–10 Myr, color-coded by age. Notably, most clusters within this age range exhibit an F300M − F335M color index close to zero. The red and orange curves indicate $+3\sigma$ and $+5\sigma$ in color dispersion, respectively. The dashed horizontal lines indicate the adopted F335M (light blue) and F300M (pink) detection limits for the PAH emitter sample, derived from 5σ measurements relative to the mean obtained via random apertures (see Section 4.1). The plots are organized by the galaxies' increasing distance from the upper left corner to the bottom right.

supergiants emerge), and 3–5 Myr old clusters with attenuation $A_V \gtrsim 1$ have optical colors that become easily confused with the 5–10 Myr population. The UV-optical colors of clusters $\leqslant$3 Myr are also highly degenerate. Further investigation is required to determine if there really are some >5 Myr old clusters with extended PAH emission timescales and unique features, or if their ages were simply determined incorrectly.

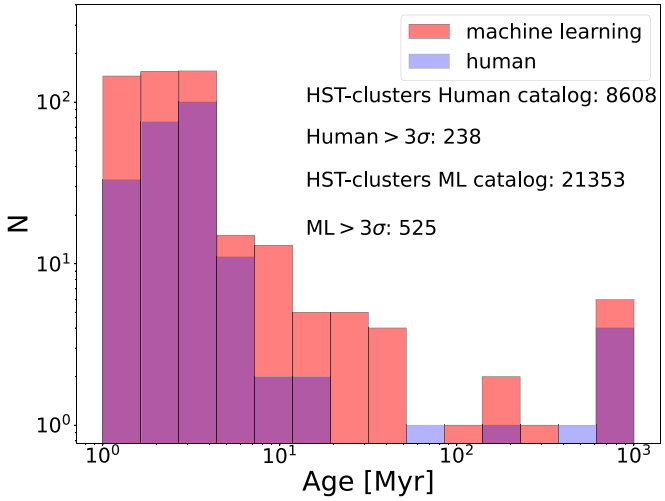

Figure 13. Age histograms for the PHANGS-HST clusters from D. Maschmann et al. (2024) with ages determined via SED fitting from D. Thilker et al. (2024) with F300M − F335M > 3σ.

6.2. Luminosity Functions

In Figure 14, we present the F200W luminosity functions (LFs) for the PAH emitters, together with the LFs for HST clusters younger than 3 Myr in black and the entire sample of objects detected in the F335M image in gray. The bright end of the HST cluster LF is 2 mag more luminous and extends to ∼−14 mag. The LF of all F335M objects shows that objects of this magnitude and brighter are detected using our method, even though they are not selected as PAH emitters. This rules out the possibility that the difference is due to a source detection issue. The LF can be described to first order by a power-law distribution, denoted as $dN/dL \propto L^{-\alpha}$ (B. C. Whitmore et al. 1999; S. M. Fall 2006). The optically selected HST clusters present an LF slope of $\alpha = 2$, consistent with the value for a scale-free distribution ($\alpha = 2$) and with previous studies of star cluster LFs (e.g., S. S. Larsen 2009; B. C. Whitmore et al. 2014b; A. Adamo et al. 2017; D. O. Cook et al. 2019; M. R. Krumholz et al. 2019). However, the PAH emitters present a steeper distribution ($\alpha = 2.4$) indicating a more rapid decrease in the number of bright clusters in this band. On the upper x-axis of this plot, we also show the corresponding estimated masses as computed based on the F200W mass-to-light ratio for young clusters as described in Section 5.4.

6.3. Comparing the Spatial Distribution of PAH Emitters and HST Clusters

In the right panel of Figure 5, we compare the positions of the PAH emitters (>5σ sample, depicted in green) with young clusters (age $<10^7$ Myr, shown in pink) over the northern area of the galaxy NGC 3627. Additionally, ALMA CO(2–1) intensity contours are overlaid in blue for comparison. We observe that the PAH emitters are located at the bar end. In this area, gas is being compressed and heated, facilitating the star formation. We also observe that the PAH emitters are within the ALMA contours, suggesting that they are still associated with molecular clouds. In contrast, the young HST clusters present a more dispersed distribution. It is interesting to note that the few HST clusters within the ALMA contours are generally closer to the edges, suggesting a potential evolutionary sequence in the transition between PAH emitters and HST clusters.

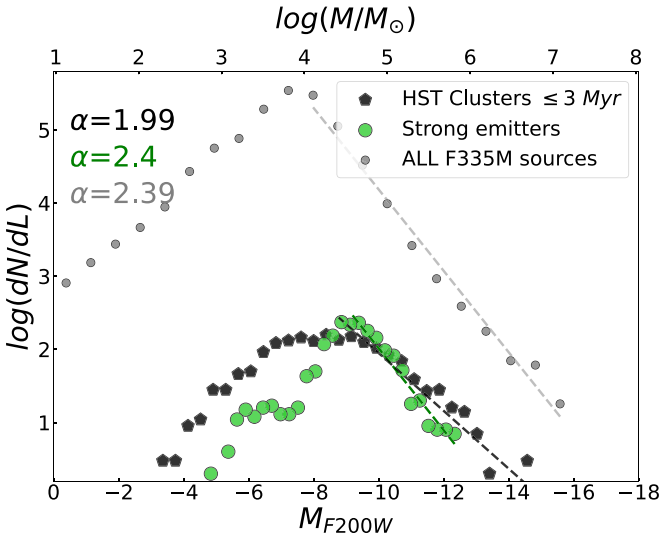

Figure 14. The LF for PAH emitters (green). We also present for comparison the LF for HST star clusters younger than 3 Myr (depicted in black) and the LF for all the sources detected over the F335M image in Section 3.1 (gray). The lines represent the best-fit linear models over the bright end of each population, with the respective fitted slope values displayed in the upper left corner. Masses derived from the method described in Section 5.4 are depicted on the upper axis. The main distinction between PAH emitters and the HST clusters are the slope at the bright end.

The 3.3 μm PAH emitters predominantly represent highly obscured, very young star-forming regions not detectable in optical wavelengths (as also illustrated by the comparison with the HST F555W imaging in Figure 9). The HST clusters close to the edges of the ALMA contours might represent optically emerging star-forming regions. Here stellar feedback plays a crucial role in dispersing the surrounding ISM. These regions can be detected at optical wavelengths but may still be partially surrounded by gas and dust. The more spread-out HST clusters are probably in a slightly more evolved state, having already swept away the material from the molecular cloud from which they formed, causing them to be very bright at bluer optical wavelengths and in the UV. While we present only one galaxy here, similar patterns are observed across the 19 galaxies in our sample.

7. Discussion

7.1. UV-IR SEDs of Compact 3.3 μm PAH Emitters and Possible Evolutionary Sequence

The 3.3 μm emission associated with young star clusters appears to persist for only a brief period, as evidenced by the near total absence of F335M color excess in HST clusters older than ∼3 Myr (Figures 11 and 12). Moreover, upon closer examination of the few oldest HST clusters found in the F300M − F335M > 3σ region of the CMDs (clusters 11 Myr to 1 Gyr; last two columns of Table 3), it was found that these clusters exhibited inaccurate SED-fitting-derived ages.

However, in this brief period when the cluster exhibits 3.3 μm emission, it will transition through various phases of its evolution, starting from heavily obscured and therefore invisible at optical wavelengths to becoming detectable in the optical and UV. To begin to study the properties of clusters through these phases, we divided our samples of PAH emitters

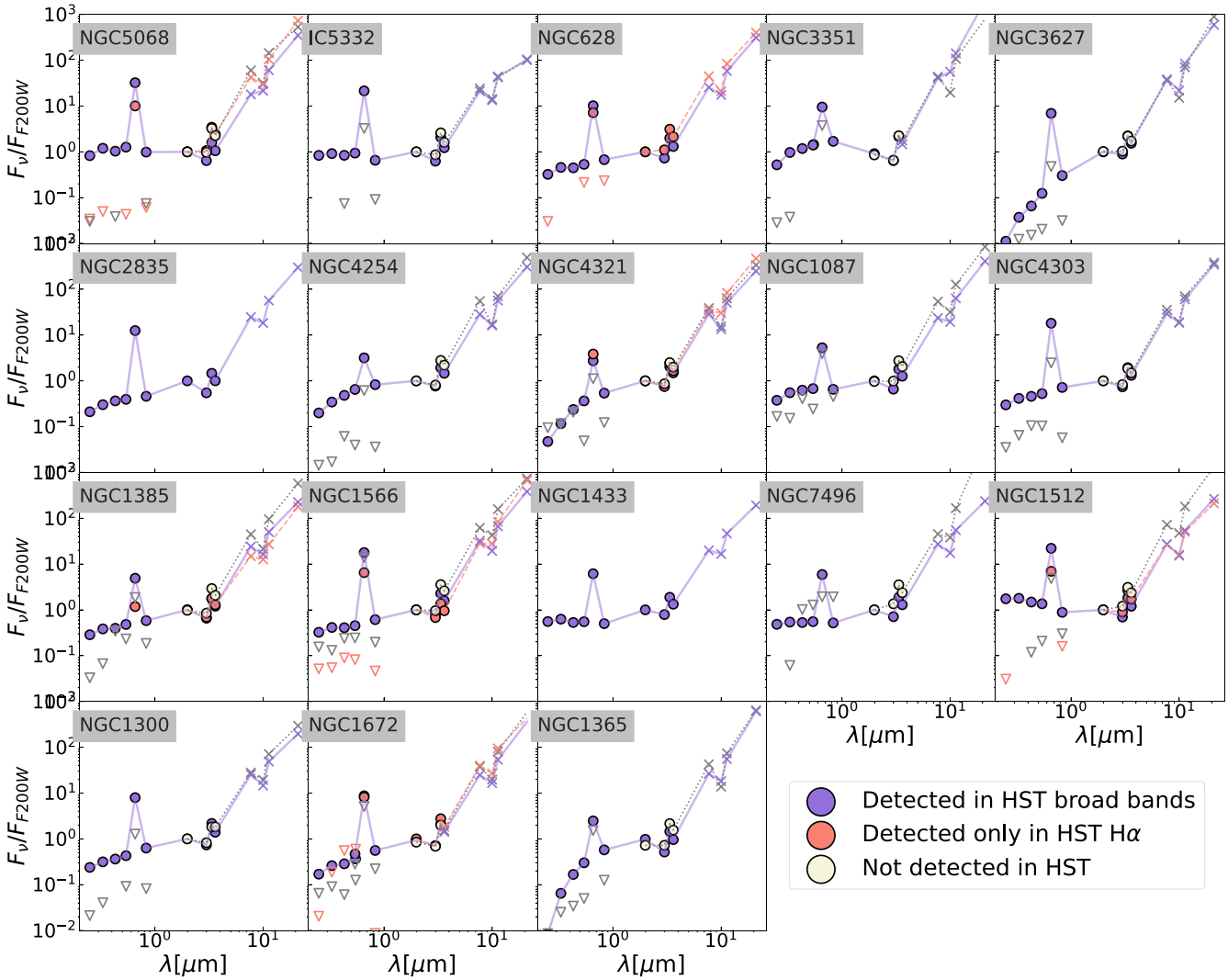

Figure 15. Median values of the SED normalized to the flux density in F200W for compact 3.3 μm PAH emitters in the "not detected in HST," "only detected in Hα," and "detected in HST" categories (see Section 7.1 for definitions of these categories). These SEDs reveal three distinct characteristics indicative of very young objects. Emission features are observed in Hα (for objects in the categories "only detected in Hα" and "detected in HST") and at 3.3 μm, and the apparent dip at 10 μm is probably due to PAH emission at the side bands 7.7 μm and 11.3 μm. We also observe a general rising flux density with wavelength. Upper limits due to nondetections are shown by open downward-pointing triangles, while the cases where there is a detection but it may be affected by neighboring sources (i.e., in the MIRI bands) are shown by crosses.

into four categories based on the detection of the objects in the UV-optical HST broad bands and the HST Hα narrow band and form their SEDs from the 14 bands of HST+JWST data available. The categories are as follows.

1. *Not detected in PHANGS-HST imaging.* S/N < 5 for aperture photometry in all five PHANGS-HST UV-optical bands (F275W, F336W, F438W, F555W, and F814W) and narrow bands (F657/8). Objects 3 and 4 in Figure 5 are in this category.
2. *Only nebular emission detected (i.e., Hα).* S/N < 5 for aperture photometry in all five HST broad bands but S/N > 5 in narrow bands. Object 5 in Figure 5 is in this category.
3. *Young sources with detection of stellar photospheric emission.* S/N > 5 for aperture photometry in at least one of the HST broad bands and Hα flux with S/N > 5. Object 1 in Figure 5 is in this category.
4. *Older sources.* S/N > 5 aperture photometry in at least two HST broad bands, but Hα flux S/N < 5.

We built the observed the SED from UV(2700 Å) to 21 μm for objects in the "not detected in HST," "only detected in Hα," and "detected in HST" categories. In Figure 15, we present median values normalized to the F200W flux density. As in Figure 6, we observe a rising IR distribution with the prominent Hα feature (in the "detected in HST" and "only Hα categories"), as well as the 3.3 μm feature and the 10 μm apparent dip. We can observe from these SEDs that objects in the first two categories ("not detected in HST" and "only detected Hα") are not found in all galaxies.

Another way to constrain the ages of the PAH emitters is to examine their Hα equivalent width (EW). EWs were estimated as $F_{\rm H\alpha+N[II]}\Delta_{\rm NB}/F_{\rm cont}$, where $F_{\rm H\alpha+N[II]}$ and $F_{\rm cont}$ were derived employing a similar methodology as described in R. Chandar et al. (2024). Briefly, we used the flux densities derived from the broadband F814W and F555W images to obtain the continuum flux contribution. To do this, we converted the flux density per unit of frequency into flux densities per unit of wavelength. Then we weighted the broadband flux densities based on the relative wavelength distance between the center of

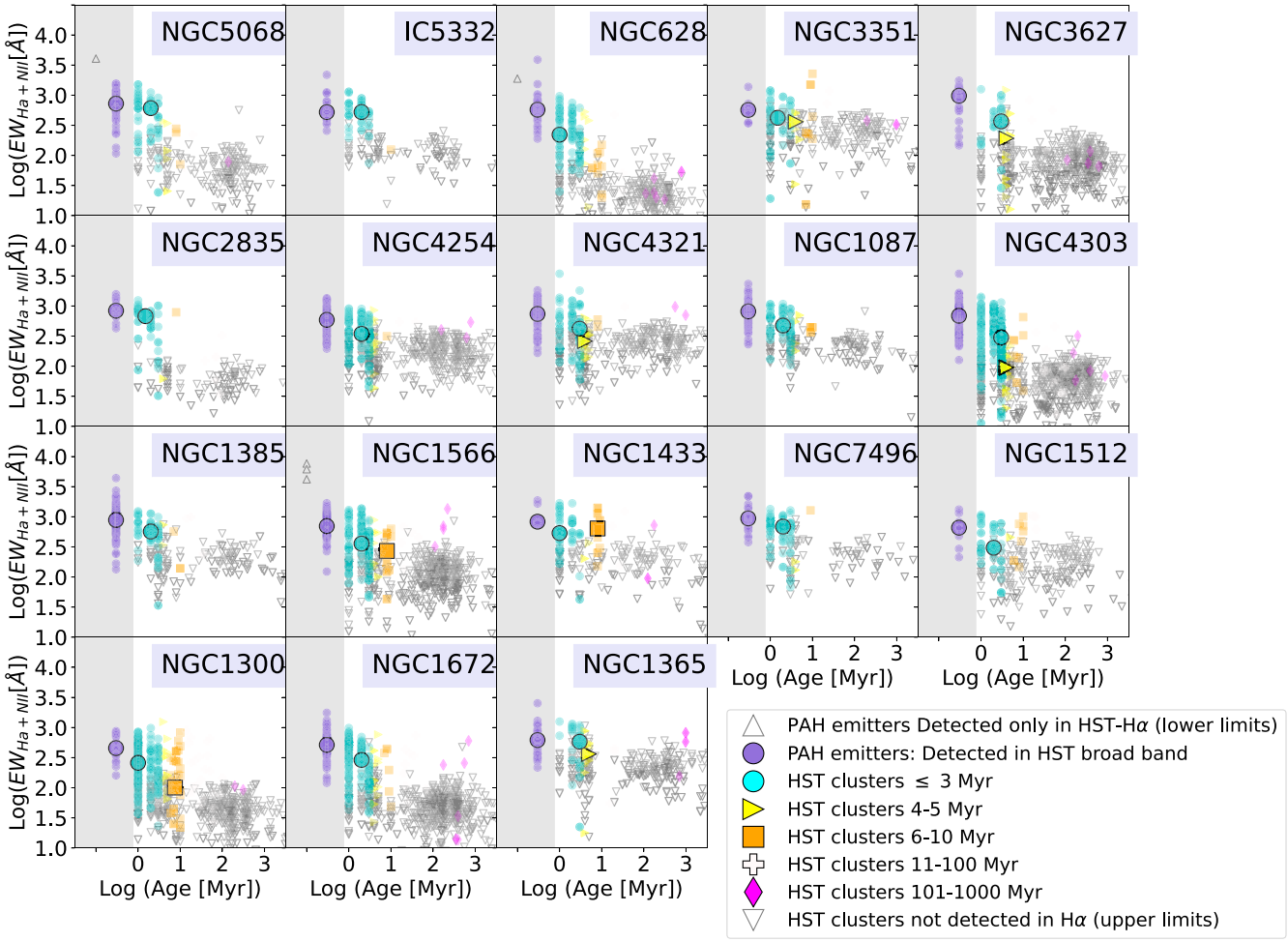

Figure 16. Evolution of Hα EW with age. The plot presents the EW derived for HST clusters and PAH emitters. The gray region denotes the absence of estimated ages for the PAH emitters; however, they are positioned to the left of the HST clusters to suggest a potential evolutionary sequence (refer to the text for details). Median values are shown with larger symbols when the sample includes at least five objects, while smaller symbols represent individual scatter. Galaxy plots are arranged by distance.

the broadband filter and the center of the narrowband filter:

$$F_{\rm cont} = F_{\rm F555W}\, W_{\rm F555W} + F_{\rm F814W}\, W_{\rm F814W}. \quad (1)$$

Next, we subtracted the continuum contribution to the narrowband density flux,

$$F_{\rm H\alpha+[NII]} = F_{\rm NB} - F_{\rm cont}, \quad (2)$$

where $F_{\rm NB}$ are the flux densities in the narrowband filter. We converted from flux densities to flux multiplying by the narrowband filter width. The flux obtained following this procedure includes contributions from Hα λ6563 as well as the [N II] doublet (λ6548, λ6583).

In Figure 16, we show the Hα + N[II] EW as a function of age for objects in PAH emitter categories 2 and 3 and only lower limits (gray upward-pointing triangles) for the "only Hα" category, as it was not possible to estimate the continuum flux since the objects were not detected in the F555W and F814W bands. Figure 16 also shows the EW for HST clusters in different age bins: ⩽3 Myr, 4–5 Myr, 6–10 Myr, 11–100 Myr, and 101–1000 Myr. Most of the HST clusters older than 3 Myr show only upper limits (gray downward-pointing triangles). The Hα EW shows a clear decline with age. In this figure, large symbols represent median values when the sample includes at least five objects, while small symbols indicate individual objects. The gray zone in the plots shows a region in which we do not have estimated ages from UV-optical broadband SED fitting. However, based on the CMDs presented in Figures 11 and 12, where only clusters younger than 3 Myr present an F335M color excess, we infer that the mean age of the 3.3 μm PAH emitter population should be younger than approximately 3 Myr. Assuming that PAH emitters detected in Hα but not detected in the HST broad bands (the "only detected in Hα" category) are in an earlier phase than those PAH emitters detected in some of the HST broad bands (the "detected in HST" category), starting from the left of the plot, we show the samples following this plausible evolutionary sequence: first the "only detected in Hα" then the "detected in HST" categories, followed by the HST clusters in increasing order of age. The EW of the PAH emitters in the gray area (again, for which we cannot estimate the age through SED fitting) is on average higher (500–1000 Å) than the optically detected PHANGS-HST clusters (200–900 Å). This provides direct evidence for them being younger than the youngest HST star clusters and that they are in an earlier phase of evolution/dust clearing.

Figure 17 shows the color F300M − F335M as a function of age for PAH emitters and HST clusters. As in Figure 16, the gray zone indicates the PAH emitter region for which we do

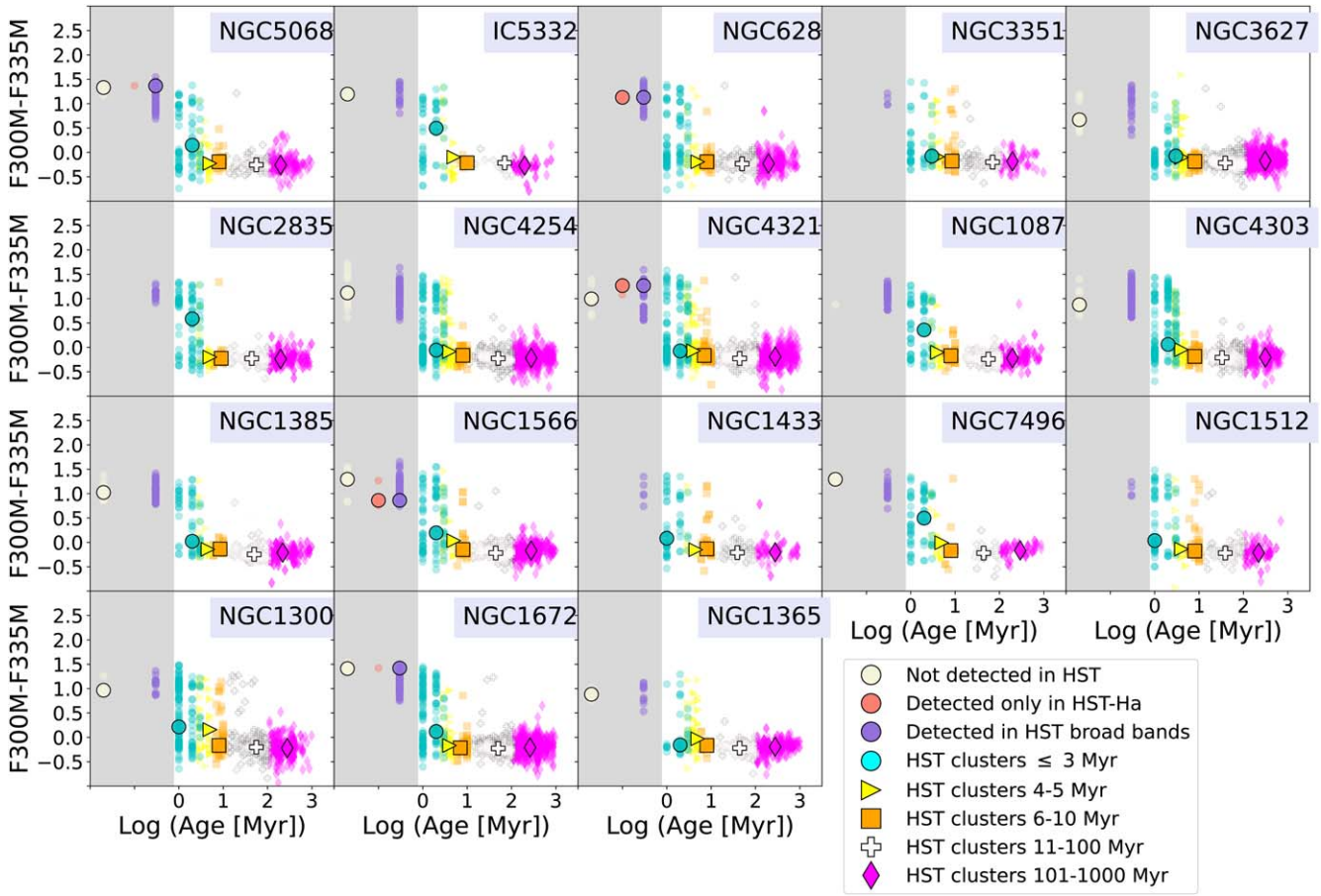

Figure 17. F300M − F335M vs. age. The gray region denotes the absence of estimated ages for the PAH emitters; however, they are positioned to the left of the HST clusters to suggest a potential evolutionary sequence (refer to the text for details). Median values are depicted with larger symbols, while smaller symbols represent individual scatter. PAH emitters in the different categories exhibit similar F300M − F335M colors, with a median around 1.5. In contrast, HST clusters older than 3 Myr show a median color around 0. HST clusters younger than 3 Myr display a wide scatter in F300M − F335M values, falling between these two median values. Galaxy plots are arranged by distance.

not have estimated ages. In contrast with the previous figure, this plot allows us to compare the "not detected in HST" objects with the other categories, and we place them to the left of the "only Hα" category to suggest the earliest phase in a possible evolutionary sequence. Interestingly, this figure shows no significant variation in the F300M − F335M color for the PAH emitters in different categories. However, it provides a complementary way of demonstrating the abrupt decay of the color for the HST clusters (as also illustrated in the CMDS in Figures 11 and 12), with F300M − F335M ~ 0 for clusters older than 3 Myr.

7.2. How Many "New" Young Star Clusters Are We Finding?

To assess the potential increase in the catalogs of young star clusters resulting from the inclusion of newly detected 3.3 μm PAH emitters, we compared the number of PHANGS-HST clusters with ages $\leqslant$3 Myr from the machine learning catalogs with the number of 3.3 μm PAH emitters $>5\sigma$ (columns (5) and (3), respectively, of Table 3).

We decided to use for the comparison the machine learning catalogs from D. Maschmann et al. (2024) (instead of the human catalogs) because they are more complete. From the HST sample, we only considered clusters in the NIRCam field of view. We also accounted for overlaps between the two data sets, using a search radius of 0.″126 (2 pixels in the F335M image). We found between 1 and 28 objects common in both samples in the different galaxies (column (7) of Table 3). Subtracting these common objects, we found that the number of "new" clusters (number of PAH emitters not previously detected in the HST catalogs) shows a large variation from galaxy to galaxy. We found as few as 10 new young clusters in NGC 1433 and as many as 224 in NGC 1385. Accounting for these compact PAH sources could increase the number of young clusters significantly compared to optical catalogs. It is important to be precise when quoting an increase factor; the number of PAH-emitting clusters not present in HST catalogs (Table 3, column (3) minus column (6) or (7)), plus the <3 Myr old HST clusters detected at 3 μm (column (4) or (5)), divided by the latter HST cluster number, is a factor ranging from 1.8× to 8.5× (median 3.3×). If one does not require a 3 μm detection to count "known young HST clusters," then the increase factor represented by the 5σ PAH emitters is between 1.1× and 3.3× (median 1.4×).

It is important to also note that these quoted numbers of "new" (embedded) clusters only refer to the bright end of the LF because of the magnitude limits for each galaxy imposed in Section 4. At fainter magnitudes, both the PAH emitter and HST catalog samples suffer from incompleteness (evident in the LF turnover in Figure 14). In addition, the PAH emitter sample may have increasing contamination from clumps of diffuse ISM. When we examined this fainter population, we

identified a substantial number of contaminants: objects with a significant F300M − F335M color excess due to an unreliable detection in F300M. This issue led us to apply the current magnitude limits. If one assumes that 50% of the fainter PAH-emitting sources are true clusters and includes those fainter sources, the number of PAH emitters increases by ∼1.3–9 times (median 3.6×) the number reported in Table 3, but there is a similar increase in the number of HST clusters as one decreases the magnitude limit—for any population with a steep LF, small changes in the completeness limits translate into horrifying changes in the number of sources in the sample. A critical science question that will need to be addressed by future work is whether the fraction of embedded clusters is different at lower masses. Establishing this clearly will require careful analysis of completeness, contamination, the stochastic population of the cluster initial mass function (IMF), and how mass-to-light ratios vary between the embedded and HST-visible populations.

7.3. Comparison with Other Studies

Recent studies have leveraged JWST's unique capabilities to observe ISM emission from optically thick regions at high resolution and advanced our understanding of the timescales over which young star clusters emerge from their dust-enshrouded molecular birth clouds. Prior to the current paper, this work focused on selected individual galaxies, similar to our early paper on NGC 7496 (M. J. Rodríguez et al. 2023). It is notable that all of these studies paint a consistent picture of these early phases of star cluster evolution, using complementary observational tracers and methods of analysis.

All studies, including the present paper, have confirmed the short dust-clearing (or PAH in particular) timescales ($\lesssim$3 Myr) reported by optical studies, which is physically significant because it indicates the importance of presupernova (i.e., "early") feedback in the star formation cycle.

J. Kim et al. (2023) use a statistical analysis to translate an observed spatial decorrelation between cold gas and SFR tracers into timescale constraints for NGC 628 at ∼1″ resolution using PHANGS-JWST MIRI F2100W, ground-based Hα narrowband, and PHANGS-ALMA CO(2–1) imaging. They find that the heavily obscured phase of star formation (i.e., only detected in CO and 21 μm and invisible in Hα emission) typically lasts for $2.3^{+2.7}_{-1.4}$ Myr. In the same galaxy, A. Pedrini et al. (2024) leverage higher-resolution NIRCam imaging (0.″15) to study the ages of clusters associated with different 3.3 μm PAH morphologies (compact, extended, and open) of ∼1000 compact H II regions identified through JWST Paα and Brα narrowband imaging. They find that compact regions, which presumably are the earliest stage in the sequence, are associated with clusters ages between 1 and 6 Myr, with a median of 4 Myr.

Several other JWST studies focus on galaxies or regions of galaxies with high star formation intensities at $z \sim 0$: the central starburst ring of NGC 3351 (J. Sun et al. 2024), the central kiloparsec of M82 (R. C. Levy et al. 2024), two cluster-rich luminous IR galaxies in the Great Observatories All Sky LIRG Survey (S. T. Linden et al. 2023, 2024), and the starbursting barred (Seyfert 2) spiral galaxy NGC 1365, which hosts the richest population of young massive clusters within ∼30 Mpc (B. C. Whitmore et al. 2023). B. C. Whitmore et al. (2023), J. Sun et al. (2024), and S. T. Linden et al. (2024) respectively report that clusters are completely obscured in the visible for 1.3 ± 0.7 Myr and either completely or partially obscured for 3.7 ± 1.1 Myr, that newly formed clusters become visible in the optical in ∼2–3 Myr, and that dust is cleared over a timescale of <3–4 Myr.

Recent studies consistently demonstrate that JWST's advanced capabilities enable the discovery of significantly more embedded young clusters than were previously cataloged using HST IR-optical detections. The key question of astrophysical significance is the fraction of young clusters that are sufficiently dust-obscured so that they cannot be detected in the optical. While definitive answers and comparison across studies require careful analysis of detection thresholds and selection criteria to enable a fair comparison of "new" embedded clusters discovered in new JWST studies, we can attempt a first preliminary synthesis by taking the results reported in recent papers at face value.

R. C. Levy et al. (2024) report that the majority (87%) of their ∼1400 massive ($>10^4$ $M_\odot$) star cluster candidates identified through NIRCam F250M imaging are new compared to previous optical catalogs, corresponding to a factor of 7–8 increase. Similarly, S. T. Linden et al. (2024) find that their sample of dust-enshrouded young massive cluster (YMCs, $N = 116$) is larger by an order of magnitude relative to previous HST studies, and 16% (an increasing factor of 1.16) of the sample is undetected at optical wavelengths.

In our previous work (M. J. Rodríguez et al. 2023), we found a total of 67 young clusters presenting 3.3 μm PAH emission in NGC 7496; 59 of them were new detections in comparison with previous HST catalogs, producing a factor of 2 increase. We also found that ∼40% of the detected sample (28 out of 67) were not detected in HST optical wavelengths. Similarly, in the present paper, we find an obscured (not optically detected) fraction of up to 40% with large variations between galaxies and depending on magnitude cuts, similar to B. C. Whitmore et al. (2023; 16 out of 30 are new) and J. Sun et al. (2024; 8 out of 14 compact millimeter continuum sources not detected by HST). In comparison with previous HST catalogs, the number of "new" detections produces an increase factor ranging between 1.8× and 8.5×, depending on the galaxy. This range is consistent with the factor reported in other studies, except for S. T. Linden et al. (2024), who found a factor of 10 (with small number statistics).

The variations between different studies arise partly from the distinct identification methods and detection thresholds employed, as mentioned above. Additionally, they reflect intrinsic differences in the systems analyzed. For example, the high inclination of M82 (R. C. Levy et al. 2024) and the dusty nature of VV 114 and NGC 3256 (S. T. Linden et al. 2023, 2024) would both lead to more extinction and thus a higher fraction of embedded clusters than the relatively face-on galaxy centers studied by B. C. Whitmore et al. (2023), J. Sun et al. (2024), and in this study.

8. Summary and Conclusions

We have expanded our initial study of dusty clusters in NGC 7496, as traced by compact 3.3 μm PAH emission (M. J. Rodríguez et al. 2023), to include the full set of 19 PHANGS-JWST spiral galaxies observed during the first year of JWST science operations (J. C. Lee et al. 2023; T. G. Williams et al. 2024). The successful deployment of JWST has enabled rapid advances in our understanding of the properties, formation, and evolution of star clusters in their

earliest dust-embedded stages, with early work focusing on individual nearby galaxies. This paper is the first, to our knowledge, to conduct a comprehensive census of dusty clusters across a representative sample of the nearby galaxy population.

1. Based on the F300M − F335M $> 5\sigma$ color excess and detection limits in both filters, we identified 1816 compact 3.3 μm PAH emitters across the 19 galaxies (green points in Figure 2), with per-galaxy counts ranging from 12 (NGC 1433) to 237 (NGC 1385) with a median of 77 (Table 3).
2. Objects with a 3σ–5σ color excess were also examined (blue points Figure 2), and these shared similar characteristics with the $>5\sigma$ emitters, though they are potentially more susceptible to contamination from continuum sources, as expected.
3. A general selection criterion for compact 3.3 μm PAH emitters was established, with a median color threshold of F300M − F335M = 0.67 at F335M = 20, though it is highly dependent on the background within each galaxy.
4. The SEDs (Figures 6 and 15) of the PAH emitters display features of very young dusty objects: red mid-IR colors, strong Hα and 3.3 μm emissions, and an apparent dip at 10 μm due to PAH emission in the flanking F770W and F1130W filters.
5. CI analysis indicates that 87% of PAH emitters resemble extended objects like star clusters (Figure 7). Examination of their spatial distribution within the host galaxy shows that they are primarily located in dust lanes, spiral arms, bar ends, inner star-forming rings, and galaxy centers (Figures 8 and 9).
6. The 3.3 μm PAH luminosities range from 2.5×10^{34} to 1.5×10^{37} erg s^{-1}, with a median of 3.5×10^{35} erg s^{-1}. Masses, estimated based on F200W mass-to-light ratios for clusters younger than 3 Myr, span from 700 to 6.5×10^{5} $M_{\odot}$, with a median of 3.4×10^{4} $M_{\odot}$ (Figure 14).
7. The F200W LF of PAH emitters (Figure 14) shows a steeper bright end compared to PHANGS-HST clusters younger than 3 Myr, indicating a rapid decrease in the number of bright clusters with 2 μm luminosity.
8. In general, only optically selected clusters from the PHANGS-HST catalog that are younger than 3 Myr display 3.3 μm emission (Figure 11), suggesting a short lifespan ($\lesssim$3 Myr) for PAH emission at the cluster scale. This provides one constraint on the duration of the dust-embedded phase of star clusters.
9. The compact PAH emitters exhibit high observed (i.e., no dust correction) Hα + [N II] EWs (median 700 Å), 1–2.8 times greater than the youngest optically detected PHANGS-HST clusters (Figure 16). This supports the conclusion that the 3.3 μm PAH emitters are on average younger than optically selected clusters and represent an earlier phase in cluster evolution.
10. The overlap between PAH emitters and optically selected clusters from PHANGS-HST catalogs is limited ($\lesssim$10%), yielding 1645 new objects across the 19 galaxies. For bright clusters in both samples, the number of embedded cluster candidates identified by PAH emission relative to HST-selected clusters younger than 3 Myr varies between a factor of 1.8× and 8.5× per galaxy (see Section 7.2 for details and caveats).
11. We compare our results with a number of recent JWST papers on dust-embedded clusters in individual nearby galaxies, which also identify significant new populations of dusty clusters and generally paint a consistent picture of a short-lived compact PAH emission and dust-embedded phase.

Future analyses of completeness and the stochastic IMF in small clusters will clarify the contribution of embedded clusters to galaxy-wide star formation. JWST photometry and the 3.3 μm PAH emission feature offer a powerful new tool for this assessment.

Acknowledgments

This work is based on observations made with the NASA/ESA/CSA James Webb Space Telescope (program #2107) and the NASA/ESA Hubble Space Telescope (program #15654 and #17126). The data were obtained from the Mikulski Archive for Space Telescopes at the Space Telescope Science Institute, which is operated by the Association of Universities for Research in Astronomy, Inc., under NASA contract NAS 5-03127 for JWST and 5-26555 for HST. The specific observations analyzed were taken from three PHANGS repositories in MAST, PHANGS-HST (L. Ubeda et al. 2021), PHANGS-CAT (D. Thilker et al. 2022a), and PHANGS-JWST (T. Williams et al. 2023). This paper makes use of the following ALMA data: ADS/JAO.ALMA#2015.00956.S. ALMA is a partnership of ESO (representing its member states), NSF (USA) and NINS (Japan), together with NRC (Canada), NSTC and ASIAA (Taiwan), and KASI (Republic of Korea), in cooperation with the Republic of Chile. The Joint ALMA Observatory is operated by ESO, AUI/NRAO and NAOJ.

R.I. acknowledges support from JWST-GO-02130.006-A.

J.S. acknowledges support by the National Aeronautics and Space Administration (NASA) through the NASA Hubble Fellowship grant HST-HF2-51544 awarded by the Space Telescope Science Institute (STScI), which is operated by the Association of Universities for Research in Astronomy, Inc., under contract NAS 5-26555.

M.B. gratefully acknowledges support from the ANID BASAL project FB210003 and from the FONDECYT regular grant 1211000.

This work was supported by the French government through the France 2030 investment plan managed by the National Research Agency (ANR) as part of the Initiative of Excellence of Université Côte d'Azur under reference number ANR-15-IDEX-01.

A.W. acknowledges UNAM and the PASPA of DGAPA.

R.C.L. acknowledges partial support for this work provided by a National Science Foundation (NSF) Astronomy and Astrophysics Postdoctoral Fellowship under award AST-2102625.

K.G. is supported by the Australian Research Council through the Discovery Early Career Researcher Award (DECRA) Fellowship (project number DE220100766) funded by the Australian Government. K.G. is supported by the Australian Research Council Centre of Excellence for All Sky Astrophysics in 3 Dimensions (ASTRO 3D) through project number CE170100013.

R.S.K. acknowledges financial support from the European Research Council via the ERC Synergy grant "ECOGAL"

(project ID 855130), from the German Excellence Strategy via the Heidelberg Cluster of Excellence (EXC 2181 - 390900948) "STRUCTURES," and from the German Ministry for Economic Affairs and Climate Action in project "MAINN" (funding ID 50OO2206). R.S.K. is grateful for computing resources provided by the Ministry of Science, Research and the Arts (MWK) of the State of Baden-Württemberg through bwHPC and the German Science Foundation (DFG) through grants INST 35/1134-1 FUGG and 35/1597-1 FUGG and also for data storage at SDS@hd funded through grants INST 35/1314-1 FUGG and INST 35/1503-1 FUGG. R.S.K. also thanks the Harvard-Smithsonian Center for Astrophysics and the Radcliffe Institute for Advanced Studies for their hospitality during his sabbatical and the 2024/25 Class of Radcliffe Fellows for a great community and highly interesting and stimulating discussions.

Facilities: JWST, HST.

Software: Astropy (Astropy Collaboration et al. 2013, 2018, 2022). This research made use of Photutils, an Astropy package for detection and photometry of astronomical sources (L. Bradley et al. 2022). AstroPy (astropy.org). The code used for source detection, photometry, and candidate selection in this work is available in our GitHub repository: https://github.com/JimenaRodriguez/Phangs-photometry.

Appendix A
IR Colors of PHANGS-HST Red Evolved Star Candidates

A population that serves as a useful point of reference for this study is red evolved stars. This population includes AGBs and red supergiants, and candidates can be readily selected from existing PHANGS-HST *V*- and *I*-band (F555W and F814W) DOLPHOT catalogs (A. Dolphin 2016; D. A. Thilker et al. 2022b). Such samples of luminous red point sources will be bright in our JWST images, and they allow us to (1) determine MIRI color criteria to help remove old stellar populations from our 3.3 μm PAH sample (Section 4.2) and (2) characterize the NIRCam CIs of point sources so that we can ascertain the compactness of the 3.3 μm PAH emitters (Section 5.1).

Selection of candidate samples of red evolved stars in each galaxy is based on DOLPHOT output parameters and location in the $V-I$ CMD (Figure 18). Specifically, we use the following DOLPHOT criteria: $S/N_{F814W} \geqslant 10$, $crowd_{F814W} \leqslant 0.01$, $PhotQualFlag_{F814W} = 0$, $OBJTYPE = 1$, $-0.025 < sharp_{F814W} \leqslant 0.01$, and $-0.15 < round_{F814W} \leqslant 0.4$, which ensures the identification of bright, uncrowded point sources that are well fit by the HST PSF. A description of these parameters can be found in the documentation for DOLPHOT.[43] The sharpness and roundness limits were adjusted as needed for each galaxy. In terms of the color–magnitude criteria, we selected sources with F814W magnitudes 3–5 mag brighter than the foreground extinction-corrected tip of the red giant branch (G. S. Anand et al. 2021) and considered only those sources with colors within the range 2 mag $\leqslant$ F555W − F814W $<$ 4 mag (Figure 18).

In Figure 19, we show the F1000W − F2100W versus F300M − F335M color–color diagram for $>5\sigma$ (green) and 3σ–5σ (blue) 3.3 μm PAH emitters. The HST red evolved star candidates are plotted if their F1000W and F2100W photometry is above the 5σ point-source limit (23.2 and 21.6, respectively; J. C. Lee et al. 2023, Table 4).

[43] Available at http://americano.dolphinsim.com/dolphot/.

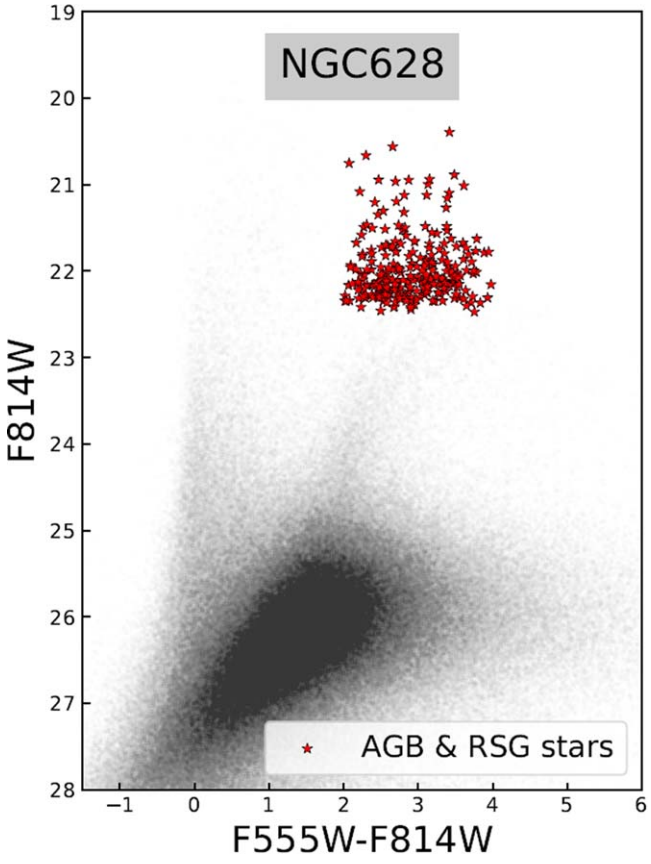

Figure 18. An example F555W − F814W vs. F814W CMD for the galaxy NGC 628. The black points are sources from the PHANGS-HST DOLPHOT catalog (D. A. Thilker et al. 2022b), while the red points show a candidate sample of red evolved stars, used in this paper to help determine MIRI criteria to remove these sources from our 3.3 μm PAH sample and to calculate the NIRCam CIs of point sources as a reference for evaluating the compactness of the 3.3 μm PAH emitters.

We observe that the vast majority of the $>5\sigma$ PAH sample has F1000W − F2100W > 1.2 ($F_{F2100W}/F_{F1000W} \geqslant 3$, shown with a horizontal line). In the nearest galaxies (first row of panels, where all galaxies have distances closer than 10 Mpc), we observe that a significant fraction of the 3σ–5σ PAH emitters fall below this value. We anticipate a higher rate of contamination from individual stars in these nearby galaxies. This is corroborated by the location of the candidate sample of evolved red stars in the nearest galaxy in the sample (NGC 5068, 5.2 Mpc), which is mostly below $F_{F2100W}/F_{F1000W} = 3$. As the galaxy distance increases, the F1000W and F2100W photometry (0.″328 and 0.″674 PSF FWHM, respectively) will not reflect individual luminous old stars or even clusters dominated by such stars, and the F1000W − F2100W color of the sources gradually becomes larger. The location of SAGE LMC stars (O. C. Jones et al. 2017) in Figure 3 clearly shows that individual stars cannot be detected in the more distant galaxies.

Nearly all sources in the 3.3 μm PAH emitter sample (~99%) are detected in F1000W and F2100W, although it should be noted that precise photometry for an individual star cluster can be challenging due to complex diffuse background emission and the coarser angular resolution. Fully optimized MIRI photometry for star clusters is beyond the scope of this work, but the point-source sensitivity limit in the least populated regions of the images (J. C. Lee et al. 2023, Table 4) motivates a fairly conservative flux ratio cut. However, the

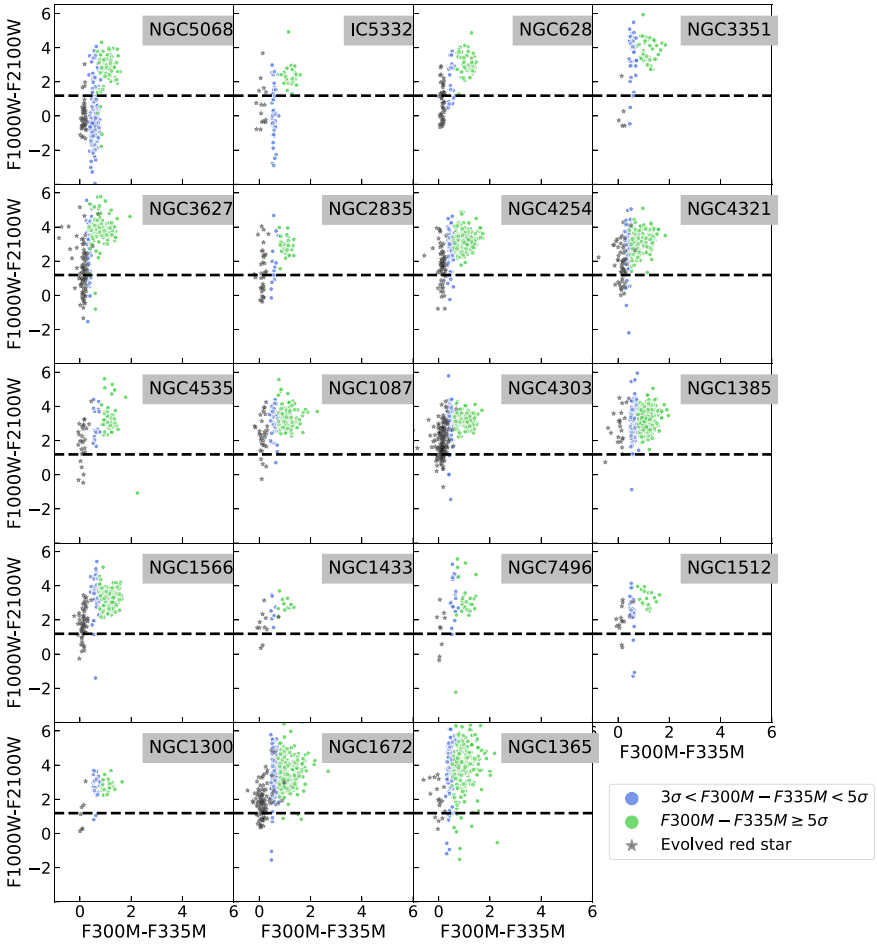

Figure 19. F1000W − F2100W vs. F300M − F335M color–color diagram for $>5\sigma$ (green) and 3σ–5σ (blue) PAH emitters. The HST candidate samples of red evolved stars are plotted if their F1000W and F2100W photometry is above their respective 5σ point-source limits (J. C. Lee et al. 2023, Table 4). The horizontal line corresponds to a value of F1000W − F2100W = 1.2 (or, equivalently, $F_{\rm F2100W}/F_{\rm F1000W} = 3$.) To remove red IR-bright stars, we exclude objects with $F_{\rm F2100W}/F_{\rm F1000W} < 3$ from the PAH emitter sample analyzed here.

F1000W and F2100W fluxes are *only* being used to exclude individual evolved stars from our sample. Confusion and inclusion of emission from neighboring sources and/or diffuse ISM will increase $F_{\rm F2100W}/F_{\rm F1000W}$, since the resolution is twice as poor at F2100W as at F1000W. Thus, cutting only those sources with low $F_{\rm F2100W}/F_{\rm F1000W}$ is valid to remove contaminants, even with the relatively poor resolution at those wavelengths.

Based on these observations, and to be conservative in the criteria to exclude individual evolved stars from the sample, we restrict our analysis to objects with a ratio of $F_{\rm F2100W}/F_{\rm F1000W} > 3$.

Appendix B
Photometric Errors

The photometric errors in the HST Hα, JWST F300M, and longer-wavelength bands were estimated using the difference between the flux density values obtained by subtracting to the 10th and 90th percentiles of the annulus, as described in Section 3.2. This method enables the capture of small variations in the local structure of the background.

In Figure 20, we present the photometric errors for the color F300M − F335M. The blue dashed line represents the 5σ detection limit derived from random aperture measurements over the F335M image. We note that this limit does not vary from galaxy to galaxy in the same way as the individual uncertainties; i.e., the variation in the detection limit across galaxies does not follow the same pattern as the average of the individual errors. This discrepancy arises because the detection limit is estimated using random apertures placed across the entire image, while the F335M detections (Section 3.1) are concentrated primarily in the main body of galaxies, where the background is brighter, resulting in higher uncertainties.

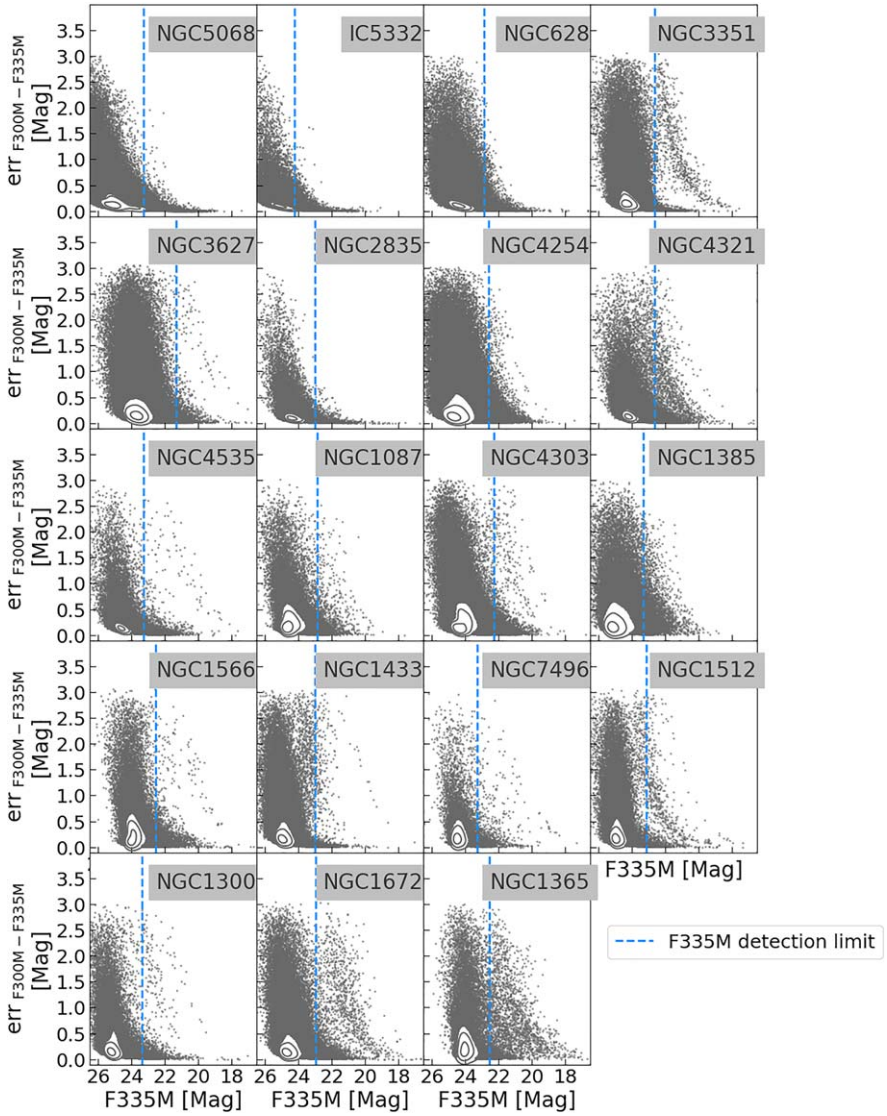

Figure 20. F300M − F335M photometric errors. The contours represent the 50th, 70th, and 90th density percentiles of all sources detected in the F335M images. Small gray dots mark regions with densities below the 50th percentile. The blue dashed line indicates the F335M detection limit, derived from random apertures (Section 4).

ORCID iDs

M. Jimena Rodríguez https://orcid.org/0000-0002-0579-6613
Janice C. Lee https://orcid.org/0000-0002-2278-9407
Remy Indebetouw https://orcid.org/0000-0002-4663-6827
B. C. Whitmore https://orcid.org/0000-0002-3784-7032
Daniel Maschmann https://orcid.org/0000-0001-6038-9511
Thomas G. Williams https://orcid.org/0000-0002-0012-2142
Rupali Chandar https://orcid.org/0000-0003-0085-4623
A. T. Barnes https://orcid.org/0000-0003-0410-4504
Oleg Y. Gnedin https://orcid.org/0000-0001-9852-9954
Karin M. Sandstrom https://orcid.org/0000-0002-4378-8534
Erik Rosolowsky https://orcid.org/0000-0002-5204-2259
Adam K. Leroy https://orcid.org/0000-0002-2545-1700
David A. Thilker https://orcid.org/0000-0002-8528-7340
Hwihyun Kim https://orcid.org/0000-0003-4770-688X
Jiayi Sun https://orcid.org/0000-0003-0378-4667
Ralf S. Klessen https://orcid.org/0000-0002-0560-3172
Brent Groves https://orcid.org/0000-0002-9768-0246
Aida Wofford https://orcid.org/0000-0001-8289-3428
Médéric Boquien https://orcid.org/0000-0003-0946-6176
Daniel A. Dale https://orcid.org/0000-0002-5782-9093
Leonardo Úbeda https://orcid.org/0000-0001-7130-2880
Kirsten L. Larson https://orcid.org/0000-0003-3917-6460
Kathryn Grasha https://orcid.org/0000-0002-3247-5321
Kelsey E. Johnson https://orcid.org/0000-0001-8348-2671
Rebecca C. Levy https://orcid.org/0000-0003-2508-2586
Frank Bigiel https://orcid.org/0000-0003-0166-9745
Hamid Hassani https://orcid.org/0000-0002-8806-6308
Sumit K. Sarbadhicary https://orcid.org/0000-0002-4781-7291

References

Adamo, A., Ryon, J. E., Messa, M., et al. 2017, ApJ, 841, 131
Anand, G. S., Lee, J. C., Van Dyk, S. D., et al. 2021, MNRAS, 501, 3621
Astropy Collaboration, Price-Whelan, A. M., Lim, P. L., Price-Whelan, A. M., et al. 2022, ApJ, 935, 167
Astropy Collaboration, Price-Whelan, A. M., Sipőz, B. M., et al. 2018, AJ, 156, 123
Astropy Collaboration, Robitaille, T. P., Tollerud, E. J., et al. 2013, A&A, 558, A33

Belfiore, F., Leroy, A. K., Williams, T. G., et al. 2023, A&A, 678, A129
Bertin, E., & Arnouts, S. 1996, A&AS, 117, 393
Bradley, L., Sipőcz, B., Robitaille, T., et al. 2022, astropy/photutils: v1.5.0, Zenodo, doi:10.5281/zenodo.6825092
Brandl, B., Sams, B. J., Bertoldi, F., et al. 1996, ApJ, 466, 254
Brown, G., & Gnedin, O. Y. 2021, MNRAS, 508, 5935
Chandar, R., Barnes, A., & Thilker, D. 2025, AJ, 169, 150
Chandar, R., Whitmore, B. C., Kim, H., et al. 2010, ApJ, 719, 966
Chevance, M., Kruijssen, J. M. D., Hygate, A. P. S., et al. 2020, MNRAS, 493, 2872
Cook, D. O., Lee, J. C., Adamo, A., et al. 2019, MNRAS, 484, 4897
Deger, S., Lee, J. C., Whitmore, B. C., et al. 2022, MNRAS, 510, 32
Dolphin, A. 2016, DOLPHOT: Stellar photometry, Astrophysics Source Code Library, ascl:1608.013
Domínguez, R., Pellegrini, E. W., Klessen, R. S., & Rahner, D. 2023, MNRAS, 520, 5600
Draine, B. T., & Hensley, B. S. 2021, ApJ, 909, 94
Emsellem, E., Schinnerer, E., Santoro, F., et al. 2022, A&A, 659, A191
Fall, S. M. 2006, ApJ, 652, 1129
Galliano, F., Dwek, E., & Chanial, P. 2008, ApJ, 672, 214
Groenewegen, M. A. T. 2022, A&A, 659, A145
Grudić, M. Y., Guszejnov, D., Hopkins, P. F., Offner, S. S. R., & Faucher-Giguère, C.-A. 2021, MNRAS, 506, 2199
Hannon, S., Lee, J. C., Whitmore, B. C., et al. 2019, MNRAS, 490, 4648
Hannon, S., Lee, J. C., Whitmore, B. C., et al. 2022, MNRAS, 512, 1294
Hannon, S., Whitmore, B. C., Lee, J. C., et al. 2023, MNRAS, 526, 2991
Hollyhead, K., Bastian, N., Adamo, A., et al. 2015, MNRAS, 449, 1106
Hopkins, P. F., Kereš, D., Oñorbe, J., et al. 2014, MNRAS, 445, 581
Imanishi, M., Nakagawa, T., Shirahata, M., Ohyama, Y., & Onaka, T. 2010, ApJ, 721, 1233
Jones, O. C., Meixner, M., Justtanont, K., & Glasse, A. 2017, ApJ, 841, 15
Kemper, F., Woods, P. M., Antoniou, V., et al. 2010, PASP, 122, 683
Kennicutt, R. C., & Evans, N. J. 2012, ARA&A, 50, 531
Kim, J., Chevance, M., Kruijssen, J. M. D., et al. 2023, ApJL, 944, L20
Kim, J. H., Im, M., Lee, H. M., et al. 2012, ApJ, 760, 120
Klessen, R. S., & Glover, S. C. O. 2016, SAAS, 43, 85
Krumholz, M. R., McKee, C. F., & Bland, J. 2019, ARA&A, 57, 227
Larsen, S. S. 2009, A&A, 494, 539
Lee, J. C., Ly, C., Spitler, L., et al. 2012, PASP, 124, 782
Lee, J. C., Sandstrom, K. M., Leroy, A. K., et al. 2023, ApJL, 944, L17
Lee, J. C., Whitmore, B. C., Thilker, D. A., et al. 2022, ApJS, 258, 10
Leger, A., D'Hendecourt, L., & Defourneau, D. 1989, A&A, 216, 148
Leroy, A. K., Schinnerer, E., Hughes, A., et al. 2021, ApJS, 257, 43
Levy, R. C., Bolatto, A. D., Mayya, D., et al. 2024, ApJL, 973, L55
Li, A. 2020, NatAs, 4, 339
Linden, S. T., Evans, A. S., Armus, L., et al. 2023, ApJL, 944, L55
Linden, S. T., Lai, T., Evans, A. S., et al. 2024, ApJL, 974, L27
Ly, C., Lee, J. C., Dale, D. A., et al. 2011, ApJ, 726, 109
Maragkoudakis, A., Peeters, E., & Ricca, A. 2023, MNRAS, 520, 5354
Martins, F., Schaerer, D., & Hillier, D. J. 2005, A&A, 436, 1049
Maschmann, D., Lee, J. C., Thilker, D. A., et al. 2024, ApJS, 273, 14
Mori, T. I., Onaka, T., Sakon, I., et al. 2014, ApJ, 784, 53
Ohsawa, R., Onaka, T., Sakon, I., et al. 2013, in Proc. of The Life Cycle of Dust in the Universe: Observations, Theory, and Laboratory Experiments (LCDU2013) (PoS), 126
Ossenkopf, V., & Henning, T. 1994, A&A, 291, 943
Pedrini, A., Adamo, A., Calzetti, D., et al. 2024, ApJ, 971, 32
Peeters, E., Martín-Hernández, N. L., Damour, F., et al. 2002, A&A, 381, 571
Portegies Zwart, S. F., McMillan, S. L. W., & Gieles, M. 2010, ARA&A, 48, 431
Rieke, G. H., & Lebofsky, M. J. 1985, ApJ, 288, 618
Rodríguez, M. J., Lee, J. C., Whitmore, B. C., et al. 2023, ApJL, 944, L26
Ryon, J. E., Gallagher, J. S., Smith, L. J., et al. 2017, ApJ, 841, 92
Sandstrom, K. M., Chastenet, J., Sutter, J., et al. 2023, ApJL, 944, L7
Schinnerer, E., & Leroy, A. K. 2024, ARA&A, 62, 369
Schutte, W. A., Tielens, A. G. G. M., & Allamandola, L. J. 1993, ApJ, 415, 397
Smith, J. D. T., Draine, B. T., Dale, D. A., et al. 2007, ApJ, 656, 770
Spoon, H. W. W., Koornneef, J., Moorwood, A. F. M., Lutz, D., & Tielens, A. G. G. M. 2000, A&A, 357, 898
Sturm, E., Lutz, D., Tran, D., et al. 2000, A&A, 358, 481
Sun, J., He, H., Batschkun, K., et al. 2024, ApJ, 967, 133
Thilker, D., Lee, J., Whitmore, B., & Maschmann, D. 2025, ApJS, in press
Thilker, D., Whitmore, B., Lee, J. C., et al. 2022a, Physics at High Angular resolution in Nearby GalaxieS - Catalogs ("PHANGS-CAT"), doi:10.17909/JRAY-9798
Thilker, D. A., Whitmore, B. C., Lee, J. C., et al. 2022b, MNRAS, 509, 4094
Tielens, A. G. G. M. 2008, ARA&A, 46, 289
Turner, J. A., Dale, D. A., Lee, J. C., et al. 2021, MNRAS, 502, 1366
Ubeda, L., Whitmore, B., Thilker, D., et al. 2021, Physics at High Angular resolution in Nearby GalaxieS - HST ("PHANGS-HST"), STScI/MAST, doi:10.17909/T9-R08F-DQ31
Wei, W., Huerta, E. A., Whitmore, B. C., et al. 2020, MNRAS, 493, 3178
Whitmore, B. C., Brogan, C., Chandar, R., et al. 2014a, ApJ, 795, 156
Whitmore, B. C., Chandar, R., Bowers, A. S., et al. 2014b, AJ, 147, 78
Whitmore, B. C., Chandar, R., Rodrìguez, M. J., et al. 2023, ApJL, 944, L14
Whitmore, B. C., Lee, J. C., Chandar, R., et al. 2021, MNRAS, 506, 5294
Whitmore, B. C., Zhang, Q., Leitherer, C., et al. 1999, AJ, 118, 1551
Williams, T., Egorov, O., Rosolowsky, E., et al. 2023, Physics at High Angular resolution in Nearby GalaxieS - JWST ("PHANGS-JWST"), STScI/MAST, doi:10.17909/EW88-JT15
Williams, T. G., Lee, J. C., Larson, K. L., et al. 2024, ApJS, 273, 13
Yamada, R., Oyabu, S., Kaneda, H., et al. 2013, PASJ, 65, 103
Zhang, L., & Ho, L. C. 2023, ApJ, 943, 60